THE JOURNAL OF PHYSICAL CHEMISTRY A

 VOLUME 107, NUMBER 11, MARCH 20, 2003

FEATURE ARTICLE

Resonant Ionization Using IR Light: A New Tool To Study the Spectroscopy and Dynamics of Gas-Phase Molecules and Clusters

Gert von Helden,*,† Deniz van Heijnsbergen,† and Gerard Meijer†,‡,§

FOM-Institute for Plasmaphysics Rijnhuizen, Edisonbaan 14, NL-3439 MN Nieuwegein, The Netherlands, Department of Molecular and Laser Physics, University of Nijmegen, Toernooiveld 1, NL-6525 ED Nijmegen, The Netherlands, and Fritz-Haber-Institut der Max-Planck-Gesellschaft, Faradayweg 4-6, D-14195 Berlin, Germany

Received: August 29, 2002; In Final Form: November 13, 2002

Resonant IR excitation of gas-phase molecules and clusters can lead to superhot species that thermally emit an electron. Monitoring the mass selected ion yield as a function of IR laser frequency yields the IR-REMPI (infrared resonance enhanced multiphoton ionization) spectrum of the molecule or cluster. Although this IR-REMPI spectrum is not the same as the linear absorption spectrum, it can be quite similar and it yields valuable information on the IR optical properties of the species investigated. In this article, the method and the necessary tools are presented. Results from experiments on fullerenes, metal carbide, metal oxide, and metal nitride clusters are shown.

1. Introduction

Over the last thirty years, lasers have revolutionized modern spectroscopy. The narrow bandwidth, high intensity, and tunability of continuous or pulsed UV and visible lasers brought us a multitude of different schemes to interrogate gas-phase molecules. Examples are laser induced fluorescence (LIF)[1] and resonance enhanced multiphoton ionization (REMPI).[2] Using these two techniques provides information about excited electronic or ionic states and their vibrational structures. LIF and REMPI detection can also be used in double (or more) resonance experiments. When one of the photons is in the infrared (IR), spectral information on IR active modes on the electronic ground-state surface of neutral molecules[3−12] can be obtained. Advances in laser technology now allow performing such experiments at wavelengths up to and beyond 10 μm, although laser fluences decrease rapidly with increasing wavelength.

When high power and fluence in the IR is desired and tunability is not much of an issue, the laser of choice is the CO_2 laser. Laser lines are available around 10 μm, continuous wave (cw) powers can be in excess of 100 W and, in pulsed mode, several Joules in nanosecond pulses can be obtained. Such lasers have been used intensely in the 70s to perform IR-multiphoton excitation (IR-MPE) and dissociation (IR-MPD) experiments on gas-phase molecules.[13] Experiments served fundamental science to investigate reaction kinetics and dynamics. IR-MPD was also tried as a tool for isotope separation.[13] In those studies, SF_6 was often used as a model system, as it has resonances around 10 μm. Recent experiments show isotopical enrichment for silicon after IR-MPD on SiH_4.[14] In another study, large amounts of ^{13}C were obtained in a CO_2 laser isotope separation process.[15]

The mechanisms of IR-MPE and IR-MPD were also theoretically investigated.[13,16−19] Models assume that the IR photons are absorbed resonantly by bright states. When the internal energy of the molecule increases, the density of vibrational states rises dramatically. The bright states couple to the abundant dark

† FOM-Institute for Plasmaphysics Rijnhuizen.
‡ University of Nijmegen.
§ Fritz-Haber-Institut der Max-Planck-Gesellschaft.

10.1021/jp021982s CCC: $25.00
Published on Web 02/27/2003

states, resulting in a shortening of the lifetime of the bright state and an increase in line width of the transition. Depending on the molecule, this effect can compensate for anharmonicities and enable the efficient absorption of multiple photons. Most of those models are, however, developed for small to medium sized molecules and it is not a priori clear in how far they are transferable to the comparatively large systems studied here. Mostly, IR-MPE leads to dissociation. There is, however, also an early[20] and a more recent[19] report where CO_2 laser IR excitation leads to the ionization of molecules. It is clear that the advantage of such a scheme is the potential for sensitive and mass selective detection.

Hot molecules have several possible pathways to cool themselves. Most molecules in low-pressure gas-phase environments will cool via the emission of photons and via dissociation. For bulk materials, the macroscopic equivalents to those molecular processes are light emission and evaporation of atoms or molecules. Many strongly bound solids such as, for example, metals have yet another cooling channel available: the thermionic emission of electrons. This process is being heavily used in technical applications, where electron-emitting filaments are used, for example, in radio tubes. The microscopic equivalent of this process is of considerable theoretical and experimental interest as thermionic electron emission requires a coupling between the nuclear motion (vibrational energy) and the electronic degrees of freedom. One of the first observations of thermionic emission occurred only at the beginning of the past decade with the observation that gas-phase fullerenes, which were heated by UV or VIS laser pulses, showed a delayed electron emission.[21,22] These results were interpreted in terms of thermionic emission where the initially excited electronic states rapidly decay to vibrationally excited states on the electronic ground-state surface. A coupling of electronic states in those hot molecules then presumably leads to ionization. Many experimental and theoretical studies[23] exists on the thermionic electron emission in fullerenes. However, the question if electron emission occurs from molecules with a statistical internal state distribution is still not settled.[23]

Essentially all organic molecules will fragment when being heated. The reason is that usually the lowest energy fragmentation channel (frequently the loss of H_2) is lower than the ionization potential. Of course, this argument is not rigorous as one needs to consider the relative rate constants of those processes that will certainly differ in their preexponential factors. Another class of gas-phase species that is known to undergo delayed (thermionic?) electron emission after UV or visible laser excitation are strongly bound gas-phase clusters. Examples include metal and metal carbide clusters,[24−27] which combine a high stability (binding energy) with relatively low ionization potentials.

We recently showed that gas-phase molecules and clusters can be efficiently excited to induce ionization using radiation from the infrared free electron laser FELIX.[28−38] When being resonant with an IR active vibrational mode of the molecule or cluster, the absorption of very many photons can take place. In fact, calculations indicate that more than 600 photons can, for example, be absorbed by a single C_{60} molecule. The internal energy of the cluster can thus rise to levels high enough to enable the thermionic emission of electrons. The absorption will only take place when being resonant with an IR active vibrational mode of the cluster. Monitoring the mass selected ion current as a function of IR frequency will thus give an IR spectrum of the species of interest. We will call this spectrum the IR resonance enhanced multiphoton ionization spectrum, or IR-REMPI, spectrum. Such a spectrum is clearly not identical to the linear absorption spectrum of the species, which, for many species investigated, is impossible to obtain. The IR-REMPI spectrum does in principle contain all the information on the linear absorption spectrum, however, and is often in appearance quite similar to it, as we will show in this paper.

The paper is organized as follows. First, introductions to the experimental techniques are given. In the next section, IR-REMPI experiments on fullerenes are presented. These results are then interpreted using theoretical models. In the second part, results from studies on metal carbide, oxide, and nitride clusters are presented.

2. Experimental Section

2.1. Free Electron Laser. An essential ingredient in the experiments is the "Free Electron Laser for Infrared eXperiments", FELIX.[39,40] In most lasers, a gas, liquid, or solid compromises the active (gain) medium and limits the wavelength range due to absorption. In a free-electron laser (FEL), however, unbound, free electrons moving at relativistic speeds through a magnetic field structure serve as the gain medium. Many excellent books and reviews on (the physics of) FELs can be found.[41] In principle, such lasers can produce photons of any wavelength. In practice, technical limitations restrict the wavelength range and most FELs operate in the IR wavelength range. A generic layout of a typical FEL is shown in Figure 1. A relativistic beam of electrons, coming from an accelerator, is injected into an assembly of alternating permanent magnets, an undulator, which is inside an optical resonator, consisting of two high-reflectivity mirrors at either side. The magnetic field in the undulator is perpendicular to the direction of the electron beam and periodically changes polarity a (large) number of times along its length. This causes a periodic deflection, a "wiggling" motion, of the electrons while the undulator is traversed. This transverse motion is quite analogous to the oscillatory motion of electrons in a stationary dipole antenna and hence will result in the emission of radiation with a frequency equal to the oscillation frequency. This oscillation frequency is given by the ratio of the velocity of the electrons to the length of one period of the path traveled by the electrons. The latter is longer than the period λ_u of the magnetic field of the undulator by a factor $(1 + K^2)$ due to the transverse motion of the electrons induced by the magnetic field; the dimensionless factor K is a measure of the strength of the magnetic field experienced by the electrons in the undulator. More precisely, the overall motion of the electrons in the undulator resembles the motion of oscillating electrons in a dipole antenna that moves with a velocity close to the speed of light. This high velocity results in a strong Doppler shift, and the wavelength of the radiation emitted in the forward direction as experienced in the laboratory frame is reduced by a factor $\approx\gamma^2$ relative to the length of the period of the undulator as traversed by the electron. As a consequence of this Doppler effect, the energy of the radiation emitted by the relativistic particles is concentrated in a narrow cone around the forward direction, sometimes referred to as the "head-light" effect. With the accelerators presently used for FELIX, the Lorentz factor γ, a measure for the total electron energy in units of its rest mass energy, can be varied over the range from 20 to 100. Given the 65 mm period of the undulator, this brings the radiation wavelength in the IR range. This radiation, referred to as spontaneous emission, is usually very weak though. This is a consequence of the fact that the electrons are typically spread out over an interval that is much larger than the radiation wavelength and will therefore not emit coherently. But on

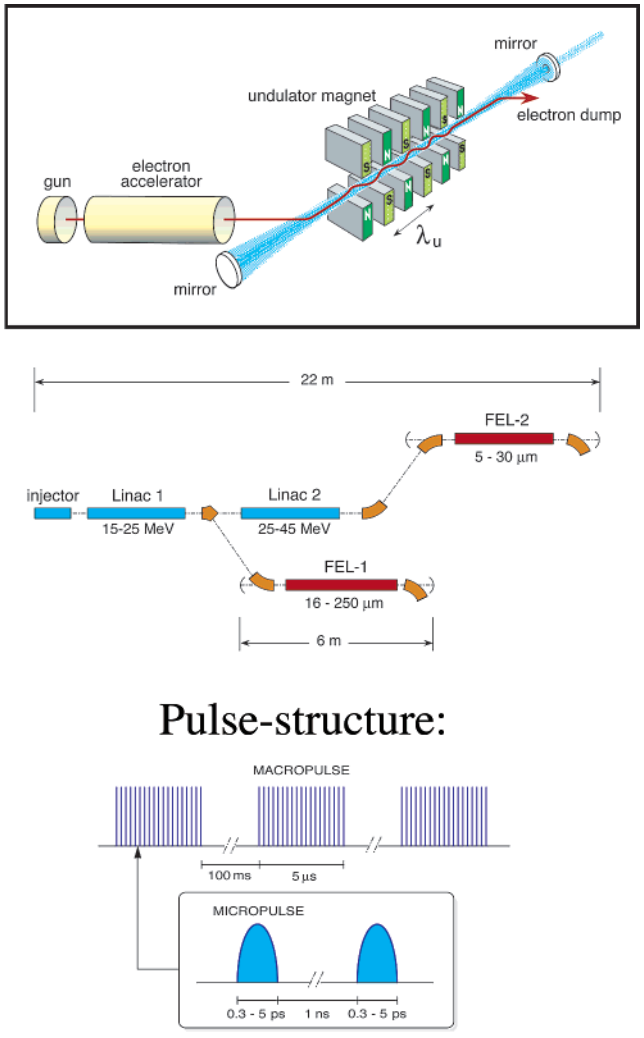

Figure 1. The top part shows a generic layout of a free electron laser. Electrons are emitted from a gun, accelerated in an accelerator, and injected into an undulator. The electrons are then dumped. Light is built up in a resonator, and a fraction of this is coupled out. In the middle, a scheme of FELIX is shown. The electron beam can either be steered into FEL-1, which is used for the long wavelength range, or the beam can be further accelerated and injected into the short wavelength FEL-2. At the bottom, the pulse structure of the light is shown schematically.

successive round trips in the resonator, this weak radiation can be amplified by fresh electrons, until saturation sets in at a power level that is typically 10^7 to 10^8 times higher than that of the spontaneous emission. It is evident that the time structure of the light in such a FEL closely mimics the time structure of the electron beam. In FELs that use (room-temperature) rf-accelerator technology the light output consists of a microsecond duration "macro-pulse", composed of a train of equidistant picosecond duration "micro-pulses", typically spaced by 1−100 ns. The macro-pulse repetition frequency is up to several tens of hertz. In FELs that use either superconducting rf-accelerators or electrostatic acceleration, continuous trains of picosecond duration micro-pulses or quasi-cw light pulses can be produced, respectively.

For experiments on gas-phase molecular systems, two key requirements for the FEL are (a) tunability and (b) high fluence on the microsecond time scale. The wavelength of the light is determined by the electron beam energy and the periodicity and strength of the magnetic field in the undulator. Any of those parameters can thus be varied to set the laser to the desired wavelength. The undulator period is usually fixed, and in most FELs, the wavelength is set by adjusting the beam energy and/or the undulator field strength. Adjusting the beam energy requires the readjustment of large parts of the electron beam optics and can be a time-consuming task. For spectroscopic experiments, where one would like to vary the wavelength rapidly, tuning is best done by adjusting the gap between the pairs of undulator magnets by means of a stepper motor. This method of tuning has the advantage that the electron beam parameters are not influenced and that a realignment of the electron beam through the accelerator and undulator is not needed.

The high fluence in a microsecond time window is required because in most gas-phase experiments, the molecules are not fixed in space but move with typical velocities of hundreds of micrometers per microsecond. Having a collimated or focused IR beam with a diameter on the order of hundreds of micrometers to millimeters means that the interaction time between a molecule and the laser is on the order of microseconds. For experiments in which multiphoton excitations of neutral gas-phase species are the objective, a high fluence per microsecond is thus important.

Presently, eight FEL-based IR facilities are operational worldwide. As the characteristics of these FELs differ considerably, so do the user programs conducted at these facilities. Due to its characteristics, FELIX is uniquely suited to do gas-phase experiments. It is continuously tunable over the 5−250 μm range. At a given setting of the beam energy, however, the tuning range is limited to about a factor 2−4 in wavelength. In practice, that means that, at a given electron beam setting, for example the range from 5 to 20 μm can be continuously scanned within a few minutes. To cover the full tuning range of FELIX, consecutive overlapping scans, each with different settings of the electron beam energy, have to be made. The macropulse length is 5 μs and the repetition rate 10 Hz. The micropulse length can be adjusted and ranges from 300 fs to several picoseconds. The bandwidth is transform limited and can range from 0.5% fwhm of the central wavelength to several percent. The micropulse repetition rate can be selected to be either 25 MHz or 1 GHz, resulting in a micropulse spacing of 40 or 1 ns, respectively. This corresponds to 1 or 40 optical pulses circulating in the 6 m long cavity of FELIX. When the experiments so require, a single micropulse can be selected using optical switching techniques. In the 1 GHz mode, the output energy can be up to 150 mJ/macropulse.

Recently, it was shown that the range between 2 and 5 μm can be covered as well by optimizing FELIX to lase on the third harmonic. This is accomplished by replacing the metal cavity mirrors by dielectric mirrors that have a high reflectivity in the desired wavelength range. Lasing on the fundamental is thus suppressed and gain is present at 3 times the photon energy. Using this approach, up to 20 mJ in a 5 μs long macropulse is obtained. In all the experiments presented here, FELIX is, however, only used on its fundamental frequency.

The IR light beam travels through an evacuated optical transport system and is delivered to the experimental setups. In the experiments described here, the distance between the outcoupling mirror and the experimental setup is about 25 m. The beam is steered through the transport system by means of gold-coated copper mirrors and is periodically refocused. The transport system is designed so as to create an image of the outcoupling mirror at the experimental user station and it is found that the beam pointing stability is very good. Typically, the IR beam is aligned before an experiment and the position

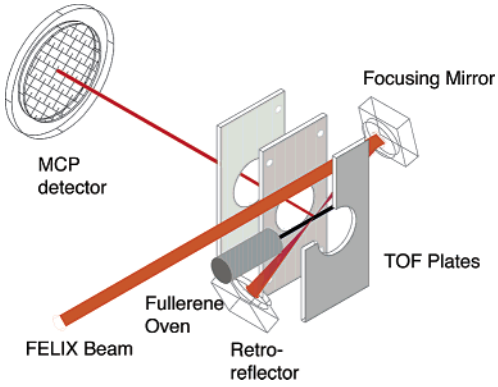

Figure 2. Fullerene setup. Fullerenes are evaporated from an oven and the effusive beam is crossed by the tightly focused FELIX beam. At some time after the FELIX pulse, the TOF plates are pulsed to high voltage and a mass spectrum is recorded. In some experiments, a reflectron TOF is used instead of the linear TOF that is shown.

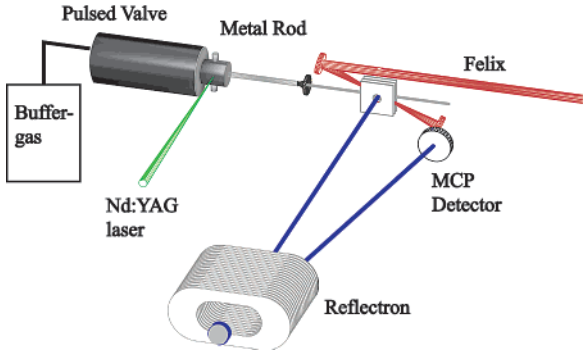

Figure 3. Cluster setup. Clusters are produced in a standard laser vaporization/supersonic expansion setup. The beam passes a skimmer, and charged clusters are deflected out using static electric fields. The neutral cluster beam is then crossed by the tightly focused FELIX beam. At some time after the FELIX pulse is over, the TOF plates are pulsed to high voltage and a mass spectrum is recorded in a standard reflectron TOF setup.

of the beam in our experiment does not drift by more than a few percent of the beam diameter during a day.

2.2. Fullerene Setup. The experimental apparatus consists of a turbo-pumped vacuum system containing a compact effusive molecular beam source and a time-of-flight (TOF) mass spectrometer, as schematically shown in Figure 2. This apparatus is directly connected to the beam delivery system of FELIX, with only a KRS5 window separating the vacuum systems. An effusive molecular beam of fullerenes is generated by evaporation of fullerene powder from a quartz oven.

The IR laser beam enters the apparatus slightly above the quartz oven and is focused by a spherical mirror with a 7.5 cm focal length in the center between the plates of the TOF mass spectrometer. A second mirror with a focal length of 3.75 cm is used as retro-reflector, effectively doubling the fluence in the focus. The focusing arm of the IR cavity makes an angle of 23° with the axis of the molecular beam, thereby lengthening the interaction time of fullerenes with the focused IR beam compared to a perpendicular geometry. The beam waist varies from approximately 60 to 200 μm in scanning FELIX from 6 to 20 μm, yielding maximum power densities of 1×10^{12} to 3×10^{10} W/cm^2 during a micropulse, respectively.

To record IR resonance enhanced multiphoton ionization (IR-REMPI) spectra of C_{60}, the TOF electrodes are pulsed to high voltage some 30 μs after the FELIX pulse, and the total number of C_{60}^+ ions is recorded as a function of IR laser wavelength. To record the time-evolution of the production of ions, the total ion signal is measured as a function of time with the voltage on the TOF electrodes being constantly on (electric field of 600 V/cm in the extraction region) and the IR laser fixed in frequency on a resonance. From the measured arrival time distribution of the ions at the detector, the flight time is subtracted to obtain the "time-of-birth" (TOB) distribution. These TOB distributions are the increment in total ion signal as a function of time; i.e., they correspond to the *rate* of ion production (multiplied by the time-constant of the detection system). Though TOB's give information on the excitation and ionization processes,[29] they are, however, not further discussed here.

2.3. Cluster Machine. The clusters of interest are produced by pulsed laser vaporization from a solid metal rod in an expansion containing several percent reactant gas in a standard setup. A scheme of the setup is shown in Figure 3. About 20−30 mJ of a frequency doubled Nd:YAG laser (Spectra Physics DCR 11) is focused on the metal surface. The metal rod can have a diameter of 6 or 12 mm and is rotated and translated to regularly expose a fresh spot on the surface. Gas from a pulsed valve (R. M. Jordan Inc.) quenches the laser plasma, clustering and chemical reactions occur, and the clusters and carrier gas expand into vacuum. When experiments are performed on metal carbides, 5% CH_4 (or $^{13}CH_4$) is seeded in argon. For metal oxides, 1−5% O_2 in argon is used and for experiments on metal nitrides, 1−5% N_2 in argon is used. Although clustering is more efficient using He as buffer gas, it is chosen to use Ar, as it produces slower beams and clusters thus have a longer interaction time with FELIX. The beam is skimmed and enters the region between the acceleration plates of a reflectron time-of-flight (TOF) mass spectrometer (R. M. Jordan Inc.) that is 20 cm downstream from the cluster source. Ions produced in the source plasma are blocked directly after the skimmer with an electric field (500−1000 V/cm) perpendicular to the molecular beam.

The optical arrangement for coupling in the IR beam is similar to the arrangement used in the fullerene experiments. The FELIX beam enters the chamber above the axis of the molecular beam and is focused on the cluster beam using a 7.5 cm focal length gold mirror. The laser beam is focused back using a 3.75 cm focal length mirror. The particles in the molecular beam move with a typical velocity of 600 m/s. The IR laser beam focus is, depending on wavelength, between tens of microns to several hundreds of microns in size. The clusters will thus not be exposed to the entire FELIX macropulse but see only up to 1 μs of it.

Typically, the acceleration plates are pulsed to high voltage 3−5 μs after the end of the FELIX pulse. TOF spectra are recorded on a digital storage oscilloscope and are transferred to a computer. The whole experiment, including the tuning of the FELIX radiation, is controlled by a set of LabView routines.

3. Results and Discussion

3.1. Infrared Excitation of Gas-Phase Fullerenes. *3.1.1. Excitation of C_{60}.* Pure C_{60} (Hoechst, "Super Gold Grade" C_{60}, purity > 99.9%) is evaporated from the quartz oven kept at temperatures between 700 and 850 K. FELIX is focused on this effusive beam with an optical arrangement as described in section 2.2. At some wavelengths in the range 5−30 μm, strong signals resulting from C_{60}^+ can be observed. The ion signal is mass analyzed by pulsing the electrodes of the TOF mass spectrometer some 30 μs after FELIX to high voltage.

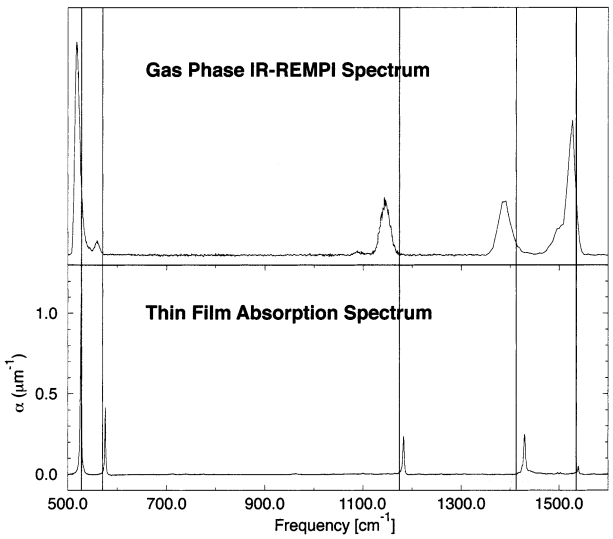

Figure 4. The top part shows the experimental IR-REMPI spectrum of fullerene C_{60}. This spectrum can be compared to the linear absorption spectrum of a C_{60} film, shown in the lower part. Black vertical lines show the positions of the IR emission bands of gas-phase C_{60} at 875 K.

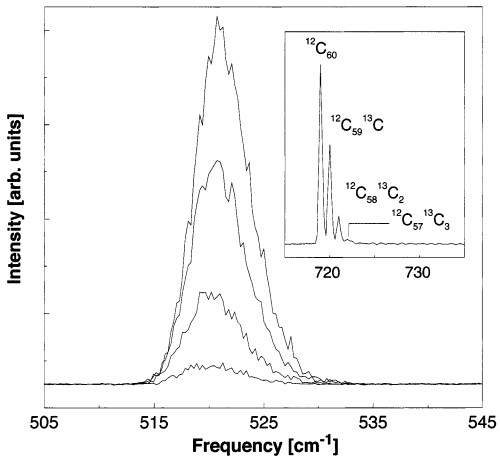

Figure 5. Shown is the IR-REMPI line around 520 cm^{-1} for C_{60} with different isotopomers. The spectra are recorded by monitoring the mass spectrum in the inset as a function of IR laser frequency. The most intense line is the one of $^{12}C_{60}$ and the weakest is of $^{12}C_{57}{}^{13}C_3$.

At the FELIX power levels used in the experiment, signals from fragments, such as $C_{58}{}^+$ (loss of C_2), are always very minor compared to the parent signal. Monitoring the amount of parent ions as a function of wavelength yields the IR-REMPI spectrum of the neutral parent. In Figure 4, the IR-REMPI spectrum of gas-phase C_{60} is shown. Clearly, several peaks can be recognized. Between the peaks, on the baseline, no ion signal is observed—not even at the maximum power levels of FELIX. The observation of ions after IR excitation is at first glance very surprising. C_{60} is known to undergo thermionic emission after heating using UV or visible lasers,[21,22] but for this process to be efficient, however, its internal energy has to be substantially higher than its ionization potential. Calculations indicate that in order for thermionic emission to fall in the experimental microsecond time window, the internal energy of the molecule has to be well above 30 eV.[42] On the strongest resonance, near 520 cm^{-1}, this implies that more than 500 photons need to be absorbed by a single gas-phase molecule in a single macropulse of FELIX!

This IR-REMPI spectrum can be compared to the linear-IR absorption spectrum of a thin film of solid C_{60} recorded at room temperature, shown in the lower trace of Figure 4. This linear absorption spectrum shows peaks at the four well-known IR active modes of C_{60}, plus one combination band at 1540 cm^{-1}.[43,44] Clearly, all peaks in the IR-REMPI spectrum have their counterparts in the linear absorption spectrum. All peaks in the IR-REMPI spectrum are shifted to the red, compared to the linear absorption spectrum. A priori it is not clear if it is useful to compare the IR-REMPI spectrum to the linear absorption spectrum of C_{60} solid. Due to molecular interactions in the solid, line positions could be shifted and selection rules could be not as strict, due to the formal reduction of symmetry. A better comparison might be with the IR emission spectrum of hot gas-phase C_{60}. Positions of the emission lines of C_{60}[45] at a temperature of 875 K are indicated as red lines in Figure 4. Clearly, the positions of the emission lines are shifted to the red compared to the linear absorption spectrum of the solid and the peak positions in the IR-REMPI spectrum are even further shifted to the red. When the relative peak intensities in the two different spectra are compared, one difficulty is the normalization in the IR-REMPI spectrum because the IR laser fluence will change when scanning the laser. If the C_{60} ion signal would depend linearly on IR laser fluence, one could just divide the $C_{60}{}^+$ signal by the laser fluence to get a normalized spectrum. Because, however, the C_{60} ion signal depends highly nonlinearly on the IR fluence, such a normalization is problematic. In Figure 4, we choose to present the raw data, without any normalization, and it should be noted that while this spectrum is recorded, the FELIX fluence varies much less than a factor of 2 over the scan range shown. A comparison of the relative peak intensities in both spectra can thus only be qualitative. Largely, the relative intensities in the two spectra are similar. The two exceptions are the IR-REMPI peaks at 560 and 1527 cm^{-1} where the relative intensity in the IR-REMPI spectrum is much smaller for the first peak and much larger for the second peak than expected from the linear absorption spectrum.

The position of the IR active mode in the molecule will shift to longer wavelength with increasing internal excitation of the molecule, due to anharmonicities. For efficient excitation, the IR laser has to be resonant with the IR active mode all the way from the initially relatively "cold" molecules leaving the oven up to the very hot molecules that are about to thermally eject an electron. When the anharmonicity in a mode is too large, efficient excitation cannot occur and a line then appears weak or is not present at all in the IR-REMPI spectrum. In the experiment, there is a correlation between the relative intensity of a peak and its shift in the IR-REMPI spectrum, compared to either the linear absorption or the IR emission spectrum: the larger the shift of a peak, the lower its intensity in the IR-REMPI spectrum. A detailed explanation will follow in the theoretical description of the excitation process (section 3.1.3).

When a reflectron TOF instrument is used for mass analysis, the mass resolution is sufficient to distinguish C_{60} ions that differ in isotopic composition and the IR-REMPI spectra of those different species can be measured. When carbon has its natural isotope distribution, many C_{60} molecules will contain one or more ^{13}C atoms. With a natural abundance of 1.12% for ^{13}C, only 52% of the C_{60} molecules contain 60 atoms ^{12}C, 34% contain one atom ^{13}C, 11% two ^{13}C atoms, and 2.2% three ^{13}C atoms. Four ^{13}C atoms are contained in only 0.4% of the C_{60} molecules and the mass peak at $m/z = 724$ is too weak to be observable in our experiment. In the inset of Figure 5, a high-resolution mass spectrum of $C_{60}{}^+$ is shown when exciting at 520 cm^{-1}. The corresponding IR-REMPI peaks of the different

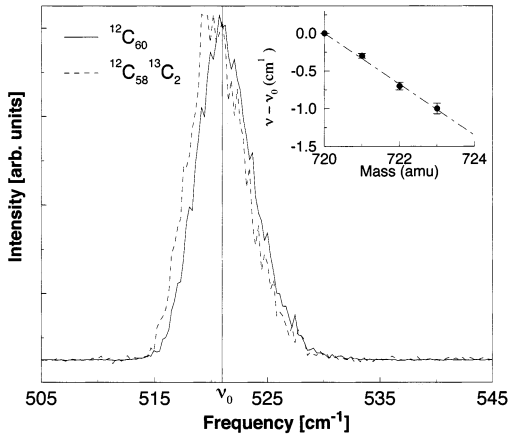

Figure 6. Shown is the IR-REMPI line around 520 cm^{-1} for $^{12}C_{60}$ and $^{12}C_{58}{}^{13}C_2$, scaled to the same height. In the inset, the observed shift in the peak position of C_{60} is shown for four different isotopic compositions.

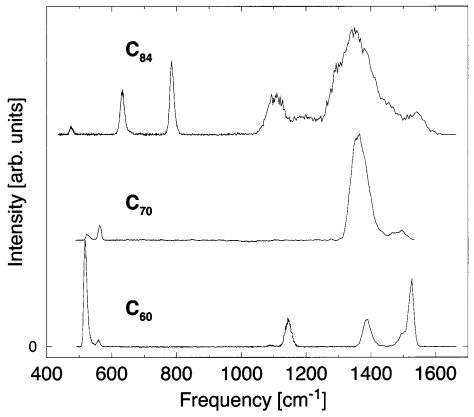

Figure 7. IR-REMPI spectra for C_{60}, C_{70}, and C_{84}.

isotopomers are shown in the figure. The strongest peak corresponds to $^{12}C_{60}$, and the weakest IR-REMPI peak, to $^{12}C_{57}{}^{13}C_3$. In Figure 6, the lines for $^{12}C_{60}$ and $^{12}C_{58}{}^{13}C_2$ are compared. A clear shift toward lower frequencies is apparent for the $^{12}C_{58}{}^{13}C_{12}$. In the inset, the peak positions relative to $^{12}C_{60}$ are shown for all isotopomers. As expected, the peak positions shift to lower frequencies when heavy isotopes are present. This shift is small, however. It ranges from approximately -0.23 cm^{-1} for the cluster containing one ^{13}C to -0.78 cm^{-1} for clusters containing three ^{13}C.

For a diatomic molecule, the changes in line position are easy to understand as the vibrational frequency is proportional to $\mu^{-0.5}$, where μ is the reduced mass. In polyatomic molecules, the situation is not as clear-cut because the reduced mass depends on vibrational mode and the motion of the atoms. For pure $^{12}C_{60}$ the reduced mass is for all vibrational modes 12. Diagonalizing a semiempirical (PM3) force constant matrix with one carbon atom replaced by a ^{13}C atom yields reduced masses that range from 12.000 to 12.11 and the specific shift of a line is critically dependent on the vibrational mode. For $^{12}C_{60}$ the position of the (3-fold degenerate) T_{1u} IR resonance is calculated to be at 557 cm^{-1}. In the one ^{13}C containing molecule, the line is calculated to split with two modes within 0.04 cm^{-1} of the original line (red. mass = 12.00) and one mode red shifted by 0.95 cm^{-1} (red. mass = 12.03). Adding two-thirds of the experimental line of $^{12}C_{60}$ to one-third of that line that is red shifted by 0.95 cm^{-1} gives, when scaled in intensity, a line that is in position and width indistinguishable from the observed line of $^{12}C_{59}{}^{13}C$.

The situation becomes significantly more complex when two ^{13}C atoms are present in one molecule. As they will be incorporated statistically, many possible isomers will result, each having possibly different line positions. However, the situation becomes simple again for $^{13}C_{60}$. There, all lines are shifted by a factor of $\sqrt{12/13}$, approximately 4%.[46] If we now do a linear interpolation between $^{13}C_{60}$ and $^{12}C_{60}$, we obtain a shift of $^1/_{15}$% per ^{13}C atom. At 520 cm^{-1}, this corresponds to 0.3 cm^{-1} per ^{13}C atom—in good agreement with the observations here. A detailed and more accurate analysis of this problem is, however, beyond the scope of this paper.

3.1.2. IR-REMPI Spectra of Higher Fullerenes. The IR-REMPI method combined with mass selective detection is ideally suited to obtain IR spectra of species that are only present as a mixture with other substances. Samples that are intrinsically hard to purify are fullerenes. Although C_{60} and C_{70} can be separated from other larger fullerenes quite straightforwardly, separation is difficult for higher fullerenes that can only be purified with very large effort. Compared to C_{60} and C_{70}, much less is thus known about the structures of fullerenes with more than 70 atoms. In the group of higher fullerenes, C_{84} received the most attention, because it is the easiest to produce higher fullerene. In addition to the difficulty of separating the fullerenes based on the number of carbon atoms, most of them also contain an isomeric mixture that is often difficult to separate. For some, the isomers that fulfill the isolated pentagon rule (IPR) are cataloged by Fowler.[47] Whereas C_{60} and C_{70} possess only one IPR fullerene, 24 different IPR structures are possible for C_{84}. For larger fullerenes, the number of possible IPR isomers increases dramatically. Soon after the first report on the isolation of the higher fullerene C_{84} [48] a considerable experimental and theoretical effort has been launched toward elucidating its structure(s). On the basis of NMR experiments,[48,49] it is now agreed upon that samples mostly contain two isomers, one isomer with D_2 and one with D_{2d} symmetry.

The experimental approach is the same as in the experiments on C_{60}. To obtain the C_{70} spectrum, a sample of pure C_{70} and, to obtain the C_{84} spectrum, a sample of "higher fullerenes" (both MER Corporation) are placed in the oven. The "higher fullerenes" sample contains 30% C_{84}, with the next most abundant fullerene less that 15%. Less than 1 mg of sample is found to allow several hours of stable operation. In Figure 7, IR-REMPI spectra of C_{70} and C_{84} are shown and compared to the IR-REMPI spectrum of C_{60} (as also shown in Figure 4).

Surprisingly, in the spectrum of C_{70}, fewer lines are observed than in the spectrum of C_{60}. Peaks are observed at 525, 563, 1360, and 1480 cm^{-1}. However, all lines besides the line at 563 cm^{-1} are found to be broad and asymmetric, so that they are likely caused by several resonances. C_{70} in its D_{5h} symmetry has 31 IR allowed modes, 10 of A_2'' and 21 of E_1' symmetry. About 10 of those lines are strong in the IR absorption spectrum[43] and are found between 458 and 674 cm^{-1}, at 795 and 1134 cm^{-1}, and between 1414 and 1460 cm^{-1}. It appears that in the IR-REMPI spectrum, only the strongest modes are found and the modes, for example, at 795 and 1134 cm^{-1} are not observed. The broad peaks at 1360 and 1480 cm^{-1} are the red shifted counterparts of the structure found in the absorption spectrum between 1414 and 1460 cm^{-1}. The peaks at 525 and 563 cm^{-1} likely correspond to the strong IR absorption features at 535 and 578 cm^{-1}.

The C_{84} spectrum is very different and exhibits a much richer structure than the C_{60} spectrum. It consist of three peaks at 475, 632, and 784 cm^{-1}, followed by a series of partially unresolved

peaks, ranging from 1050 to 1600 cm^{-1}. It should be noted that the peak at 475 cm^{-1} is the lowest frequency IR-REMPI peak obtained so far. In order for the molecule to acquire the energy necessary for efficient autoionization (30−50 eV[42]) more than 800 photons have to be absorbed by a single molecule at that frequency.

The IR-REMPI spectrum of C_{84} has been compared to theoretical predictions.[30] There, the experimental spectrum is compared to spectra of two isomers, the D_2 and the D_{2d} isomer. The two calculated spectra are found to be very similar to each other and in very good agreement with the experimental spectrum. A more detailed account of the experiments on C_{84} can be found elsewhere.[30]

3.1.3. Excitation Dynamics. For molecules to thermally ionize with a reasonable probability, the rate constant for thermal electron emission has to compete with rate constants of other cooling processes. In low pressure (collision-free) environments, these cooling channels are the emission of light (radiative cooling) and the emission of particles (evaporative cooling). In the case of evaporative cooling, the particles emitted can be atoms, molecular fragments, or electrons. All channels compete with each other. Which of the channels is important in a particular experiment depends strongly on the molecule, its degree of excitation, and the relevant experimental time scale.

Radiative cooling can be approximately described by the Stefan−Boltzmann law. The emission intensity scales then as T.[4] The rate constants for fragmentation or ionization can to a first approximation be estimated from the Arrhenius equation and scales with temperature as $\propto e^{-E_a/k_bT}$, with E_a being the activation energy for dissociation or ionization, k_b the Boltzmann constant, and T the vibrational temperature. Radiation will thus dominate at low internal energies, but at high energies it will not be able to compete with dissociation and ionization, of which the rates increase much more rapidly with increasing energy. When the excitation of the molecules or ions occurs via IR multiphoton excitation to sufficiently high levels, the density of vibrational quantum states can be very high—the molecule reaches a vibrational quasi continuum. The time evolution in phase space can then be highly statistical and can be described by statistical models. The rate constant for thermionic emission at a certain internal energy can be estimated using the well-known RRKM expression as the ratio of the sum of available product (separate ion plus electron) quantum sates to the density of states in the reactant, divided by Planck's constant. Detailed investigations of the ionization process can be found elsewhere.[23]

Because C_{60} has 174 vibrational degrees of freedom, its density of states is enormous, even at moderate excitation energies. A plot of the vibrational density of states as a function of energy is shown in Figure 8. The state density is evaluated using the Beyer−Swinehart algorithm using published vibrational frequencies.[50] At an internal energy of 7.6 eV, for example, 10^{65} states per wavenumber are present. Thus, when the vibrational energy is just at the ionization potential, very many vibrational states exist; however, only a few are leading to ionization. In order for the ionization rate constant to reach the experimental time window, the internal energy has to be substantially higher than the ionization potential.

As is estimated,[42] 30−50 eV of internal energy in a C_{60} molecule is required for the rate constant of ionization to reach the experimental time window. When C_{60} leaves the oven at 800 K, the mean internal energy is 5 eV (Figure 8). At an excitation energy of 520 cm^{-1}, the required additional 25−45 eV of energy corresponds to 390−700 photons, which all have to be absorbed resonantly by a single molecule.

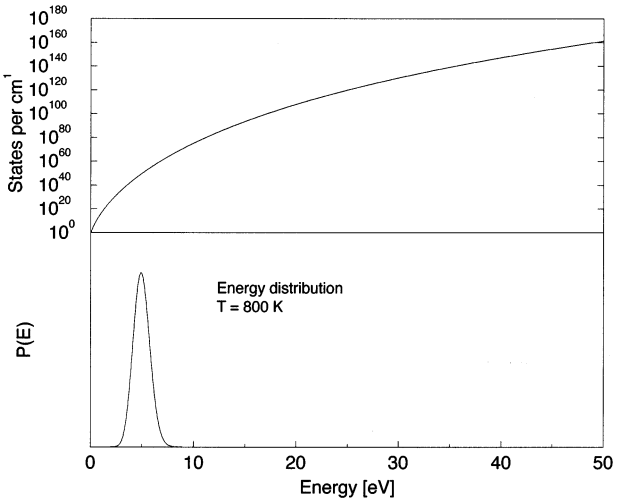

Figure 8. In the top part, the density of vibrational states of C_{60} is shown as a function of internal energy. The calculated energy distribution for thermal C_{60} at 800 K is shown in the lower part of the figure.

When C_{60} effuses from the oven at 800 K, its mean internal energy is with 39 000 cm^{-1} rather high, but with 10^{48} states/cm^{-1} at this internal energy, the density of states is even more remarkable. The density of states rapidly climbs to much larger values at higher energies (see Figure 8), and the coupling between these many states due to vibrational anharmonicities results in very fast IVR. It is therefore safe to assume that the IVR process is much faster than the rate of photon absorption. The vibrational energy is then at any time statistically distributed over the vibrational degrees of freedom and the excitation process can be described using a statistical approach.[13] It is also expected that, due to the high density of states and the coupling between them, coherent excitation effects, such as chirped induced adiabatic passage, are not important in the experiments described here.

We now go on to derive a model for the absorption process and compare the results to the experiment.[31] The individual levels in the ladder of levels that are in resonance with the excitation laser field are enumerated by the index $i = 0, ..., \infty$ and their energy E_i can be expressed as $E_i = \hbar\omega i$ where ω is the angular frequency of the laser radiation. The dynamics of the population distribution can be described by the kinetic equations

$$dn_i/dt = F_{i+1,i} + F_{i-1,i} - F_{i,i+1} - F_{i,i-1} \quad (1)$$

where n_i is the population of the ith level and $F_{i,j}$ is the rate of the population flow between levels i and j induced by the laser. $F_{i,j}$ can be written as

$$F_{i,j} = \frac{I}{\hbar\omega}\sigma_{i,j}n_i \quad (2)$$

where I is the laser intensity and $\sigma_{i,j}$ is the absorption cross-section of the $i \rightarrow j$ transition. The spectrally integrated absorption cross-section $A_{i,j}$ is defined by

$$A_{i,j} = \int \sigma_{i,j}(\omega)\, d\omega = 4\pi\omega_{res}\frac{d_{i,j}^{\ 2}}{\hbar c} \quad (3)$$

where $d_{i,j}$ is the dipole moment matrix element of the transition and ω_{res} is the frequency of the molecular resonance. We assume that transitions in the ladder of levels are characterized by the statistically averaged values $\langle d_{i,j}^2 \rangle$ of the appropriate matrix

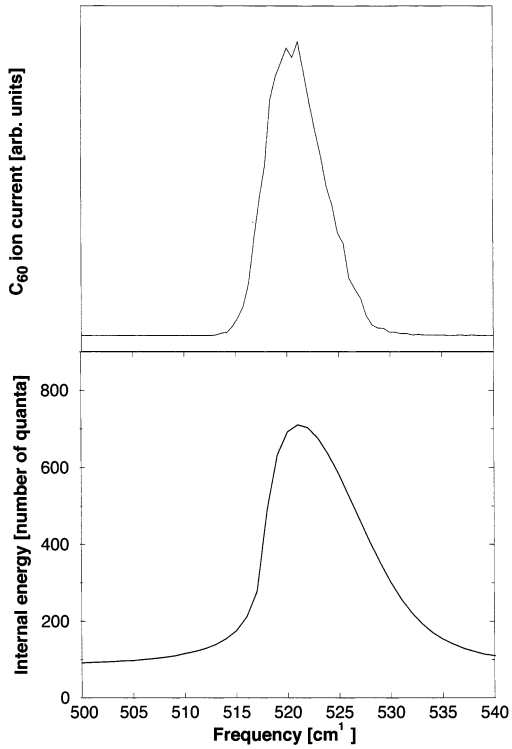

Figure 9. The top part shows the C_{60}^+ ion current as a function of FELIX frequency. In the lower part, the calculated internal energy, expressed in the mean number of absorbed 520 cm^{-1} photons, is shown as a function of FELIX frequency.

elements. The relation between up and down transitions must satisfy the principle of detailed balance

$$\sigma_{i,i+1}/\sigma_{i+1,i} = A_{i,i+1}/A_{i+1,i} = g_{i+1}/g_i \quad (4)$$

with g_i the density of states at level i. The absorption cross-section of a vibrational band is given by

$$\sigma_{i,j}(\omega) = A_{i,j} f(\omega - \omega_{res}) \quad (5)$$

where $f(\omega - \omega_{res})$ is a normalized Lorentzian line shape function, in which broadening of the line due to IVR and shifts of the resonant frequency due to anharmonicities are incorporated. The rotational contribution is neglected in view of the small rotational constant of C_{60}. We assume that both the width of the Lorentzian (fwhm), $\Gamma(E_i)$, and the resonant frequency depend linearly on the internal energy E_i as $\Gamma(E_i) = ai$ and $\omega_{res} = \omega_0 + bi$. The expression for $\sigma_{i,j}(\omega)$ has to be convoluted with the spectral profile of the excitation radiation, which is assumed to be a Lorentzian as well.

The parameters a and b are estimated from temperature-dependent emission studies on gas-phase C_{60} [45] as $a = 0.0165$ cm^{-1} per quantum and $b = -0.017$ cm^{-1} per quantum for the IR active mode with $\omega_0 = 527$ cm^{-1}. The spectrally integrated absorption cross-section of this mode is obtained from FTIR data of solid C_{60} as 2.8×10^{-17} cm.

In the calculations, an initial thermal distribution of populations is taken. The laser pulse is taken as a block function in time with the same time-integrated fluence as used in the experiment. The set of differential equations (1) is solved numerically using the Runge−Kutta-Merson algorithm.

In Figure 9, the experimental IR-REMPI spectrum of C_{60} around 520 cm^{-1} is shown (top trace) together with the excitation calculated using the model (bottom trace). In the calculation, a laser fluence of 5 J/cm^2 and a laser bandwidth of 2.5 cm^{-1} is assumed. It should be stressed that all parameters in the calculations are fixed and no adjustable parameters are used. The nonzero baseline in the calculation results from the thermal energy of the hot C_{60} effusing from the oven. The calculations show that the excitation of C_{60} can indeed be substantial: more than 700 photons of 520 cm^{-1} in a single molecule! The calculated excitation profile exhibits a maximum at a frequency of 521 cm^{-1}, in good agreement with the maximum of the IR-REMPI peak at about 520 cm^{-1}. Interestingly, this maximum at 521 cm^{-1} is obtained from a calculation that includes a value of 527 cm^{-1} as a value for the 0 K absorption line position. Another striking feature is the asymmetry in the calculated excitation profile as well as in the experimental IR-REMPI line shape in Figure 9. In both spectra, the peak rises faster on the low-frequency side and decays slower on the high-frequency side. Qualitatively, this effect can be understood by the changes in absorption profile when the internal energy of C_{60} increases and is described in detail in a previous publication.[31]

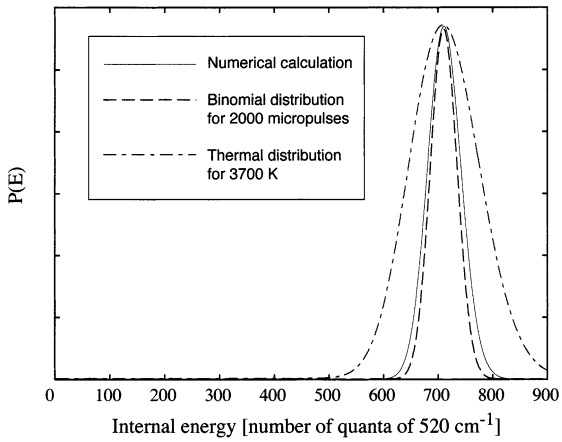

Figure 10. Calculated internal energy distribution of an ensemble of C_{60} molecules excited at 520 cm^{-1} shown as a solid line. Shown with a dashed line is a binomial distribution. A thermal distribution with the same average energy is shown as a dot-dashed line.

In Figure 9, the mean number of absorbed photons is shown as a function of excitation energy. Of course, not all molecules absorb the same number of photons and a distribution of energies is associated with each excitation energy. The distribution resulting from the numerical calculation is shown as a solid line in Figure 10. It is interesting to compare this distribution to a much simpler model: a binomial distribution of the number of absorbed photons. Such a distribution is shown as a dashed line in Figure 10. This distribution is based upon the molecules being exposed to $n = 2000$ micropulses, and for each micopulse, the absorption probability p is 0.355, independent of the number of photons already absorbed. The resulting binomial distribution is somewhat narrower than the distribution obtained from the numerical model; however, this distribution is based on a zero Kelvin initial thermal distribution whereas the numerical simulation includes an initial temperature distribution of 800 K. Clearly, such a binomial distribution serves as a good approximation for the more elaborate full numerical simulation of the excitation process. In calculations of MPE of the SF_6 molecule, a similar Gaussian distribution is obtained, using a slightly different model.[17]

When the absorption probability p is small, the binomial distribution goes over into a Poisson distribution. The standard variation of such a Poisson distribution is given by $\sigma_n = \sqrt{\bar{n}}$,

where $\bar{n} = np$ is the mean number of absorbed photons (710 in Figure 10). In terms of energy, a Poisson distribution has a mean energy of

$$\bar{E} = \bar{n}h\nu \tag{6}$$

and a standard deviation of

$$\sigma_e = \sqrt{\bar{n}}h\nu \tag{7}$$

A distribution with a mean energy of 710 photons at 520 cm^{-1} (46 eV) has thus a standard deviation of only 1.7 eV. This can be compared to the excitation with 9 photons of 5.0 eV energy (248 nm, KrF excimer laser), in which the standard deviation of the energy distribution created is 15 eV—almost an order of magnitude wider.

After a molecule is excited in the multiple photon absorption process, one or more cooling pathways are energetically open. Which one a particular molecule with some specific internal energy will take depends on the probabilities (rate constants) leading to the different product channels. For fragmentation and ionization, these probabilities will depend (near) exponentially on the internal energy. At most energies, there will be thus one rate constant for a particular channel that dominates. Further, when the energy is not too high, the molecule will be able to follow one and only one product channel within the experimental time frame. In other words, if one excites and would obtain a microcanonical ensemble, the energy of the molecules could be chosen such that the molecules would only ionize and not fragment, or only fragment and not ionize.

If the excitation results in a wide distribution of internal energies, and one wants to observe products with some reasonable probability, many molecules will be in the hot wing of the distribution and will be able to, for example, fragment after undergoing thermal ionization. This is expected to be the case when exciting with 5.0 eV photons to 45 eV mean internal energy, where a substantial amount of molecules will have 60 eV or more of internal energy. And with UV photons this is almost unavoidable; when it is decided to use a lower excitation to avoid the hot tail and fragmentation, the total ionization yield will be too low. On the other hand, when exciting with low energy photons, the resulting energy distribution will be so narrow that one can tune the mean of the distribution such that one has efficient ionization and hardly any molecules have enough internal energy to undergo fragmentation afterward. This results in fragmentation-free mass spectra. This point is of particular importance in the cluster experiments where, when ionization and fragmentation would both be occurring, it would not be clear which neutral molecule is the absorbing species for a particular observed ion.

3.2. IR Excitation of Gas-Phase Nanoclusters. Most fullerenes distinguish themselves from other molecules by the fact that they are very strongly bound and that their ionization potential is low compared to the activation barrier for dissociation. Vibrationally hot fullerenes can thus evaporate an electron instead of fragmenting. The only other class of gas-phase species where thermionic (delayed) emission is known to occur are strongly bound clusters containing highly refractory metals.

Such clusters can be generated using the laser vaporization techniques described in section 2.3. When the vaporization of the metal rod occurs in a gas mixture containing a neutral rare gas and a reactant gas, mixed cluster materials, such as metal carbide, oxide, or nitride clusters, can be produced. Charged particles that are generated are deflected by electric fields and the neutral cluster beam reaches the interaction region with FELIX. When FELIX is resonant with a vibrational mode of the cluster, many photons can be absorbed and the cluster can subsequently thermally ionize. This will only happen to very stable clusters, as less stable clusters will fragment, rather than ionize and the observation of ionic signal is thus indicative of the high stability of the corresponding cluster. In the forthcoming sections, results form experiments on metal carbide, oxide, and nitride clusters are presented.

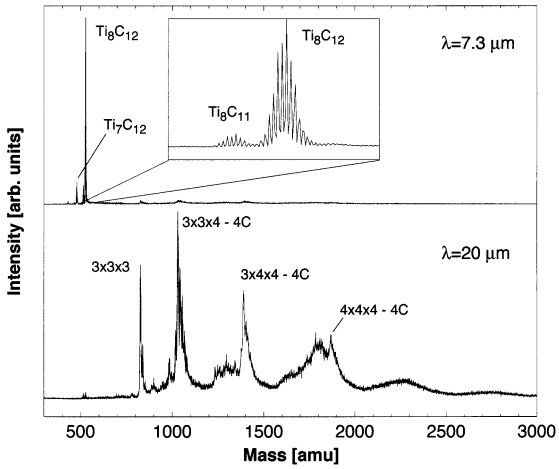

Figure 11. Mass spectrum of titanium carbide cluster ions when exciting at 7.3 μm (top part) and 20 μm (bottom spectrum). The inset above the top trace shows the Ti_8C_{11} and Ti_8C_{12} peak zoomed in, showing the isotopic distribution.

3.2.1. Metal Carbides. Bulk titanium carbide is metallic in character. The structure of bulk TiC and similar metal carbides can be thought of as a regular metal lattice in which the octahedral holes are intercalated by carbon atoms. When the size of the octahedral hole is large enough to accommodate a carbon atom without distorting the metal lattice, the intercalation is energetically favored, and very stable metal carbides result that have a metal-to-carbon ratio of 1:1 and a fcc crystal structure. This is the case for metals in which the atom radius is above about 1.3 Å, like Ti, Zr, Hf, V, Nb, Ta, Mo, and W. Their carbides are characterized by very high melting points (3000−4000 K), high hardness (between topas and diamond), and electrical conductivity. When the atom radius is smaller, as is the case for example for Cr, Mn, Fe, Co, and Ni, the corresponding carbides often have a stoichiometry that is different from 1:1 and are significantly less stable. Observations in cluster beams are in line with this, as the first group of carbides are produced with ease whereas for the second group carbides in cluster beams are hard to form and, if they form, the positions of the corresponding peaks in the mass spectra do not agree with the positions expected for nanocrystalline structures.

3.2.1.1. Mass Spectra. Metal carbide clusters can be generated by vaporization of the corresponding metal in a gas mixture of 95% argon and 5% CH_4. Here, results from studies on titanium, vanadium, niobium, and zirconium carbide clusters are presented. Mass spectra of titanium carbide clusters excited at two different wavelengths are shown in Figure 11. When the clusters are excited at a wavelength of 7.3 μm (top trace), several small clusters are observed. The largest peak (or better group of peaks) results from clusters having the composition Ti_8C_{12}. Less intense peaks are observed for Ti_8C_{11} as well as for Ti_7C_{12}. In the inset, an expanded view of the region around Ti_8C_{12} and Ti_8C_{11} is shown. Clearly, fine structure can be observed that arises from the natural isotope distribution of titanium. The observed isotope distribution is virtually indistinguishable from a simulated

distribution, strongly supporting the stoichiometries indicated in the figures. In addition, experiments have been performed using $^{13}CH_4$ as the reactant gas. The resulting mass peaks show the expected shifts. Experiments using CD_4 show unshifted mass spectra, indicating that no hydrogen atoms are incorporated into the cluster structure. $Ti_8C_{12}^+$ has previously been observed to be abundant ("magic") in mass spectra.[51] When other ionization methods are used, the smaller clusters Ti_8C_{11} as well as Ti_7C_{12} are, however, not observed to be special. When a small peak is observed at the low mass side of a large peak, it is possible that the lower mass peak does not result from ionization of the corresponding neutral cluster but from fragmentation of a higher mass ionic cluster. The $Ti_7C_{12}^+$ peak is observed to disappear at lower laser powers, and further, $Ti_7C_{12}^+$ is a known fragment from the dissociation of $Ti_8C_{12}^+$. It is thus very likely that, in the experiments presented here, this peak is caused by fragmentation of $Ti_8C_{12}^+$ as well. $Ti_8C_{11}^+$ on the other hand appears to result from an original stable neutral that independently undergoes thermionic emission when excited. This mass peak shows a power dependence very similar to the one of $Ti_8C_{12}^+$, and further, the IR spectrum of Ti_8C_{11} is distinctively different from that of Ti_8C_{12} (vide infra).

In the lower trace, a mass spectrum after excitation at 20 μm is shown. Clearly, the mass distribution is very different from the one observed after 7.3 μm excitation. Hardly any $Ti_8C_{12}^+$ is found, and all mass peaks result from larger clusters. The lowest mass peak with significant intensity results from $Ti_{14}C_{13}^+$. An intense peak from this ion, when looking at ions coming directly from the source, has been observed before[52,53] and is assigned to a cubic cluster consisting of $3 \times 3 \times 3$ atoms having a structure similar to that of bulk TiC, which has a fcc (NaCl like) structure. The larger clusters observed in the mass spectrum follow the patterns that can be observed from direct ions from a TiC cluster source[52,53] and those observed in the IR-REMPI ionization of vanadium carbide clusters.[36] Prominent peaks are observed at masses that correspond to those of ideal or near ideal cubes of atoms. In the mass spectrum presented, the isotopic distribution of Ti and the limited mass resolution of the mass spectrometer of 1000−2000 results in a not fully resolved mass spectrum. Nonetheless, distinct groups of peaks are observed having rather sharp maxima. These maxima appear at masses corresponding to cubes of $3 \times 3 \times 4$, $3 \times 4 \times 4$, and $4 \times 4 \times 4$ atoms, all however shifted 48 amu toward lower masses. They thus could correspond to clusters having one titanium atom less than the ideal clusters. They could, however, also correspond to clusters having four carbon atom less than the ideal cluster. Whereas a $Ti_{14}C_{13}$ cluster with the dimensions $3 \times 3 \times 3$ atoms will have all eight corners occupied by metal atoms, this is no longer possible if one or more sides have an even number of atoms. In this case, four corner atoms will be occupied by metal atoms and four by carbon atoms. In experiments on vanadium carbide clusters, clusters with carbon atom vacancies, presumably at the corners, are observed.[36] For vanadium carbide, it is also observed that other cubic structures, such as $3 \times 3 \times 5$ or $3 \times 4 \times 5$ atom clusters are present. There, the $3 \times 4 \times 5$ structure shows again a tendency to form clusters that lack four carbon atoms. The $3 \times 3 \times 5$ structure on the other hand can have all corners occupied with metal atoms and the cluster prefers to form the ideal structure.[36] In the case of TiC, the complicated isotope distribution of titanium prevents us from deducing detailed information from the mass spectrum. Nonetheless, it is clear that the mass distribution when exciting at 20 μm is compatible with (defective) cubic cluster structures.

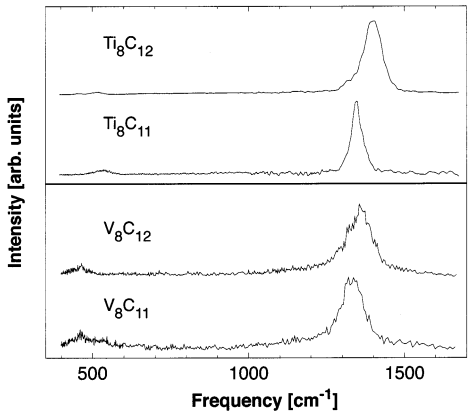

Figure 12. IR-REMPI spectra for Ti_8C_{12}, Ti_8C_{11}, V_8C_{12}, and V_8C_{11}.

3.2.1.2. Infrared Spectra. For each mass peak, its wavelength dependence can be monitored and an IR spectrum can be obtained. In Figure 12, the IR-REMPI spectra for Ti_8C_{12} and Ti_8C_{11} as well as for V_8C_{12} and V_8C_{11} are shown. The spectra are dominated by a single strong resonance, centered around 1400 cm^{-1} (7.3 μm). The ion signal for those clusters is also found at around 500 cm^{-1} (20 μm), its relative intensity there is, however, significantly less than at 1400 cm^{-1}. As described above, in order for clusters to undergo thermionic electron emission, they need to be very stable as neutrals; i.e., they need to possess high dissociation thresholds and relatively low ionization potentials. Although this is somewhat expected for Ti_8C_{12} and V_8C_{12}, it comes as a surprise for Ti_8C_{11} and V_8C_{11}. These clusters have not previously been observed to be special ("magic"), nor did anybody propose a special structure for them. The spectra of the (8,11) clusters can be compared to their (8,12) counterparts. Clearly, the spectra are very similar, but it is important to note that they are not the same. If they were the same, one could not exclude the possibility that the (8,11) clusters formed during or after the excitation/ionization process by fragmentation of (8,12) clusters. The peaks in the spectra of the (8,11) clusters are somewhat red shifted compared to the (8,12) clusters and, at least for Ti_8C_{11}, the resonance is narrower. The spectrum of the (8,12) and (8,11) clusters look very different from the spectra of the other larger titanium carbide clusters (Figure 14). This is in line with the large differences in the proposed structure of Ti_8C_{12} from the structures of the larger titanium carbide clusters. Although there is some uncertainty on the details of the structure, all proposed structures for (8,12) clusters involve C_2 units that coordinate to the metal atoms.[54−59] The IR spectra of the (8,11) clusters in Figure 12 are similar to those of Ti_8C_{12} and V_8C_{12}, indicating that the main structural motives are similar as well. In our experiments on Ti, V, Nb, and Zr carbide clusters, no larger clusters, in particular at masses that would correspond to "multicages",[60,61] with spectra similar to those in Figure 12 are observed. The only clusters with similar IR spectra are the (8,12), (8,11), and (7,12) clusters. There are indications that the observed signal at the mass of the (7,12) cluster does not result from excitation of neutral (7,12) and is instead caused by fragmentation of (8,12).

The spectrum of Ti_8C_{12} can be compared to the spectra of other (8,12) carbides. Figure 13 shows the spectra of Ti_8C_{12}, V_8C_{12}, Zr_8C_{12}, and Nb_8C_{12}. The spectra are all very similar and are dominated by a resonance that lies between 1250 cm^{-1} for Nb_8C_{12} and 1395 cm^{-1} for Ti_8C_{12}. Because the spectra are so similar, it is likely that the structures of the clusters are very similar as well. It is expected that the resonance is mainly caused by C−C stretching motion in the M_8C_{12} clusters. The calculated

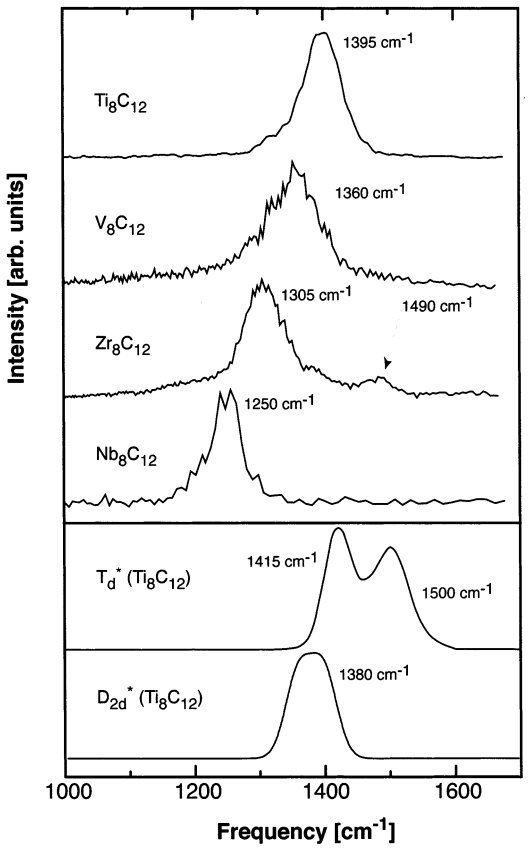

Figure 13. IR-REMPI spectra between 1000 and 1700 cm^{-1} for Ti_8C_{12}, V_8C_{12}, Zr_8C_{12}, and Nb_8C_{12}. Shown in the lower part are calculated spectra for different Ti_8C_{12} structures.[59]

C−C distance in the C_2 units in Ti_8C_{12} is between 1.32 and 1.37 Å.[59] This corresponds to a typical bond length in a C−C double bond, for which, however, a vibrational frequency of 1600−1700 cm^{-1} would be anticipated. The values observed here are closer to those anticipated for C−C single bonds. It is, however, also clear that the vibration will also contain contributions from motion of the metal atom, plus that the bonding between the two carbon atoms cannot be classified in simple terms of single or double bonds. It is observed that the resonance shifts to the blue when going from the heavier to the lighter metal atoms. Two effects will give rise to that. First, heavier atoms result in a lower reduced mass for the vibration and thus also in a red shift of the resonance. As a second effect, the bond order and bond strength of the C−C group will vary in the four M_8C_{12} molecules and a stronger (and thus stiffer) bond will shift the frequency up. The observed shift in vibrational frequencies is rather continuous, whereas the change in mass, on going from the first row transition metals Ti and V to the second row transition metals Zr and Nb, is rather discontinuous. It is thus more likely that the shift in vibrational frequency is caused by an increased strength in the C−C bond for the M_8C_{12} compounds containing the lighter metal atoms.

The experimental spectrum of Ti_8C_{12} can be compared to theoretical spectra. At the bottom of Figure 13, two spectra of Ti_8C_{12} that are calculated by Pacheco and co-workers[59] are shown. In their work, several different Ti_8C_{12} isomers are considered. The lowest two isomers are of (slightly distorted) T_d and D_{2d} symmetry. Their calculated spectra are reproduced in Figure 13. The T_d* isomer is calculated to be the lowest energy isomer, 1.8 eV below the second highest isomer with (near) D_{2d} symmetry. When the calculated spectra are compared to the experiment in Figure 13, it is clear that the D_{2d}* isomer agrees very well with the experiment. The T_d* isomer is calculated to have two peaks, which is clearly not observed in the case of Ti_8C_{12}.

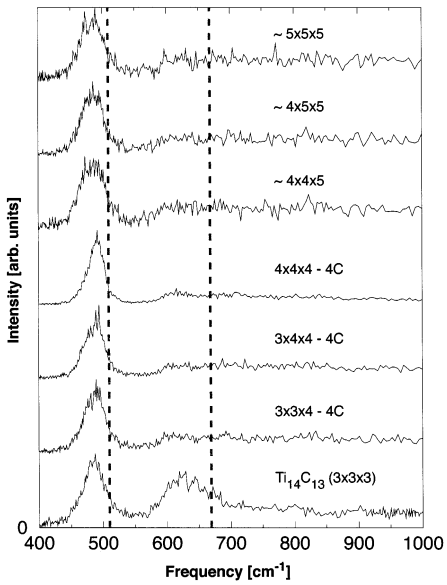

Figure 14. IR-REMPI spectra of different nanocrystalline titanium carbide clusters. Shown as dashed lines are the two optically active surface phonon modes of bulk TiC, measured by HREELS.[62]

In the spectrum of Zr_8C_{12}, the main peak is observed at 1305 cm^{-1}. However, a clear second and weaker peak can be seen at 1490 cm^{-1}. Such a second peak is not observed for the other structures. In the case of Ti_8C_{12}, the lack of a second peak can lead to the conclusion that its structure is most likely a (possibly distorted) D_{2d} structure. It is now tempting to speculate that calculated spectra for V_8C_{12}, Zr_8C_{12}, and Nb_8C_{12} would look qualitatively similar to those of Ti_8C_{12} and that the presence of the second peak for Zr_8C_{12} indicates a change of symmetry for that cluster. However, further theoretical input is needed to unambiguously answer that question.

In Figure 14, IR spectra for Ti_xC_y clusters in the frequency range between 400 and 1000 cm^{-1} are shown. The mass spectra recorded when exciting in this spectral range are dominated by clusters with a very different stoichiometry than the (8,12) or (8,11) clusters. These clusters have a near 1:1 ratio of Ti/C and, as is discussed in the previous section, the distributions observed in the mass spectra that are recorded when exciting at around 500 cm^{-1} point to nanocrystalline structures. The IR spectra of all clusters are dominated by a strong resonance at 485 cm^{-1}. When going from $Ti_{14}C_{13}$ ($3 \times 3 \times 3$ atom cluster) to clusters of sizes in the range $Ti_{63}C_{62}$ ($5 \times 5 \times 5$ atoms cluster), the position of this peak does not shift to within experimental uncertainty. For $Ti_{14}C_{13}$, an additional peak at 630 cm^{-1} is observed. For larger clusters, this peak becomes weak and broad and melts into an almost constant background that persists up to 1000 cm^{-1} and beyond.

Because it is claimed that the TiC nanoparticles have a structure that is very similar to the structure of bulk TiC, their IR spectra should be compared to spectra of bulk TiC. As is mentioned before, bulk TiC is a conductor (metallic). When bulk TiC is irradiated with (IR) light, the light will interact with the conduction electrons, leading to the reflection of the incoming electromagnetic wave. This effect will effectively shield the lattice vibrations and a phonon spectrum is thus difficult to measure using IR light. An alternative method to get information on (surface) phonons of bulk samples is electron energy loss spectroscopy (EELS). Using this technique, the

entire phonon dispersion curve can be measured, including the $k = 0$ optically active phonons. The group of Oshima has done so for most of the refractory metal carbides, including TiC.[62] In Figure 14, the positions of the two optically active phonon modes of the TiC (100) surface[62] are indicated as dashed lines. Surprisingly, the peak positions observed in the spectra of TiC nanoclusters are very close to the surface phonons observed for the bulk in the EELS experiment. In the EELS experiment, it can be argued that the lower frequency line at 504 cm^{-1} corresponds to the motion of the surface carbon atoms perpendicular to the surface whereas the higher frequency mode at 653 cm^{-1} corresponds to motion of carbon atoms parallel to the surface. It is of course not clear how such a mode description can be applied to the small nanoclusters that are studied here, as many carbon atoms will be located on edges or corners. Nonetheless, it is striking how close the here observed resonances are to the bulk and it is surprising that clusters as small as $3 \times 3 \times 3$ atoms seem to have already "bridged the gap" to the bulk, at least as far as their vibrational properties are concerned.

At $Ti_{14}C_{13}$ or $V_{14}C_{13}$, the vibrational properties seem already converged to the bulk. It would thus be interesting to investigate smaller nanocrystalline clusters. Unfortunately, for titanium[32] and vanadium,[36] no ion signal for smaller nanocrystalline clusters is observed. This can have several reasons. First, it might be that there are no smaller neutral nanocrystalline clusters in the beam. This seems unlikely, as they are expected to be intermediates in the growth of the (observed) larger clusters. Another reason might be that the clusters are not excited high enough using FELIX. This could be caused by either resonances being weaker or significantly shifted from those of the bigger clusters. Or, alternatively, their anharmonicities might be significantly larger and resonances thus quickly shift out of the excitation profile of FELIX. The most likely explanation is, however, that when the small clusters are excited, they decide to evaporate neutral atoms and not electrons. When particles get smaller, their ionization potentials usually increase and their dissociation thresholds decrease. It thus might be the case that small TiC or VC nanocrystals are just not stable enough to undergo thermionic emission in the IR-REMPI experiment. Recently, in experiments of tantalum and niobium carbide clusters, IR-REMPI signal was observed for clusters as small as M_4C_4.[38] In those experiments, it is observed that the very small clusters from M_4C_4 to M_9C_9 have an IR spectrum that is significantly different from larger clusters and the bulk. Starting from $M_{10}C_{11}$, the low-frequency mode appears and, as for TiC and VC clusters, becomes the dominant mode for larger clusters.

When the TiC or VC spectrum is averaged over all cluster-sizes, the only peak that remains is the one at 485 cm^{-1}. In a previous publication,[33] this averaged spectrum of TiC nanocrystals was compared to the emission spectrum of dying stars (post-AGB objects). This comparison led to the assignment of the so-called "21 μm feature"[63] in the emission spectrum of these stars as resulting from the thermal radiation of TiC nanoparticles in their dust shell. In the meantime, spectra of the other metal carbides VC,[36] TaC,[38] and NbC[38] have been measured. For all these materials, the spectra of nanocrystals larger than $M_{14}C_{13}$ are dominated by a resonance just above 20 μm. In principle, the "21 μm feature" could thus be caused by any of the metals mentioned above, or a mixture of them. Nonetheless, TiC nanocrystals remain the most likely candidate, as they are extremely easy to produce, titanium has the highest cosmic abundance from the group of metals that produce strongly bound carbides, and further, TiC nanocrystals have been identified in meteoritic samples that are believed to have been produced near AGB stars.[64]

As mentioned before, for bulk TiC, an IR spectrum cannot be measured directly. The small particles we measure, however, do have a regular IR spectrum as one would expect for a molecule or cluster with a HOMO−LUMO gap larger than the photon energy. When the HOMO−LUMO gap would be smaller than the photon energy, electronic transitions would occur, resulting in a broad and unstructured spectrum. We can thus conclude that the particles considered here do have a band gap higher than the photon energy and are thus not yet metallic. It would be very interesting to investigate the transition to the metal using IR-REMPI and such experiments are planned in the future.

3.2.2. Metal Oxides. Many metal oxides are of great technological importance in, for example, ceramic materials, catalysis, and electronic devices. Metal oxides can have properties that change significantly with composition and stoichiometry. Their electronic properties can, for example, vary from insulators, semiconductors, metals, to even high T_c superconductors. Some of them can be produced and used as nanoparticles using wet chemical techniques. For example, nanoparticles of Al_2O_3, Sb_2O_5, CeO_2, SiO_2, SnO_2, Y_2O_3, ZnO, and ZrO_2 with sizes of several nanometers are large scale chemical products and are commercially available. Understanding the geometric and electronic structures of these small particles is of obvious importance.

Small particles of metal oxides play also an important role in the formation of cosmic dust. During the Infrared Astronomical Satellite (IRAS) and Infrared Space Observatory (ISO) space missions, IR spectra of many stellar objects have been obtained. Surprisingly, many spectra show a rich structure and many peaks have been assigned as resulting from oxide materials.[65] During identification of the carriers of spectral features, comparison is sometimes made to laboratory spectra; however, for most materials, the IR spectral properties of small particles are calculated from bulk optical constants. The validity of such a comparison is a priori not clear, and the real spectra for small and very small particles might deviate from the expected ones.

Metal oxide clusters can be investigated using IR-REMPI. Thus far, we have observed IR laser induced thermionic electron emission for magnesium, aluminum, zirconium, and titanium oxide clusters. Here, we will present results from studies on zirconium and titanium oxide clusters.

Titanium oxide has been thoroughly studied because of its importance in materials and catalysis as well as because of its interesting electronic properties. TiO_2 is naturally mainly occurring as rutile. The metal atoms have an oxidation state of +4 and TiO_2 is an insulator, which can exhibit n-type conduction when doped or slightly reduced. An oxygen deficient structure Ti_2O_3 contains the Ti atoms in a +3 oxidation state and Ti_2O_3 exhibits a temperature induced insulator to metal transition. TiO contains the Ti atoms in an +2 oxidation state and shows metallic behavior. However, TiO is significantly less stable and is difficult to obtain and study in pure form. The vibrational properties of TiO_2 bulk[66] and surface[67] have been studied intensively. It is found that the highest frequency bulk mode is around 800 cm^{-1} and the corresponding surface mode is downshifted by about 50 cm^{-1}. Defect (Ti_2O_3 containing) surfaces of titanium oxide have been studied as well[68] and it is found that modes are then slightly red shifted.

Due to the outstanding properties of ZrO_2, the structure of its bulk phase and that of small particles are the focus of an intense research effort. The melting point of ZrO_2 is around

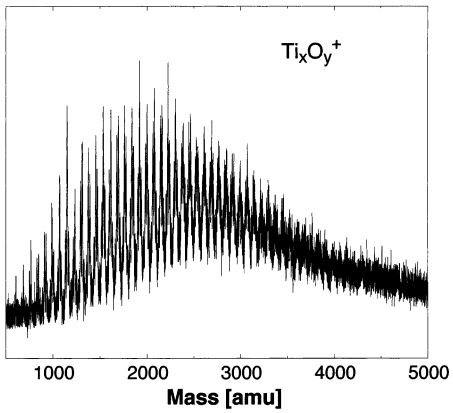

Figure 15. Mass spectrum of titanium oxide clusters after IR excitation at 750 cm^{-1}.

3000 K, its hardness is exceptionally high, and it can be an ionic conductor, leading to widespread applications in industry. The crystal structure of bulk ZrO_2 is complicated by three different structural phases that, depending on pressure, temperature, and the possible presence of small amounts of other materials, can exist. For bulk ZrO_2, the stable phase at room temperature has a monoclinic structure. Interestingly, small particles of ZrO_2 with a radius of <150 Å[69,70] are stable in the higher symmetry tetragonal phase. For bulk material, the IR spectra depend strongly on the crystal phase.[71,72] For clusters of zirconium oxide, no information on the (vibrational) structure is available. Small anionic clusters of zirconium oxide have been studied in the gas phase.[73] The clusters observed contained up to nine Zr atoms and their composition deviates significantly from that of the bulk with the number of oxygen atoms for all clusters (having more than one Zr atom) being more than twice the number of Zr atoms. When oxygen is present in a larger amount than the natural 1:2 stoichiometry, the cluster is expected to have a high electron affinity but also a high IP. In clusters with less oxygen than the 1:2 ratio, the IP is expected to be lower than in the stoichiometric cluster. However, it is also expected that the thermodynamic stability is lower. It is thus not clear which clusters one expects to observe in the IR-REMPI experiment.

3.2.2.1. Titanium Oxide Clusters. Titanium oxide clusters are generated using the techniques described in section 2.3 by using argon as a carrier gas, and seeding it with 5% O_2. A typical mass distribution when exciting with FELIX at 750 cm^{-1} can be seen in Figure 15. Large clusters, spanning to clusters heavier than $m/z = 5000$ are observed. At large masses, the mass spectrum becomes unresolved due to the wide titanium isotope distribution. The shape and center of the distribution depends strongly on source conditions. Zoomed in views are shown in Figure 16. No signal is observed at masses that correspond to $(TiO_2)_n$. An assignment of the mass spectrum is, however, not straightforward. The isotope distribution for a titanium atom is centered around 48 amu, which corresponds to the mass of three oxygen atoms. A peak in the mass spectrum at $m/z = 1072$ could thus correspond to $Ti_{14}O_{25}^+$; however also for example to $Ti_{13}O_{28}^+$ or $Ti_{15}O_{22}^+$. Nonetheless, it is clear from the figure that mass peaks occur in groups, with each group consisting of three peaks that are 16 amu apart and each group being the mass of a TiO_2 unit apart from the next group. The smallest group of peaks observed is around $m/z = 608$. There, about seven individual peaks are observed, spaced by 1 amu. No peaks 16 amu higher or lower are observed. The pattern observed is consistent with the presence of several titanium atoms. The limited signal-to-noise however does not yield a basis for a fit

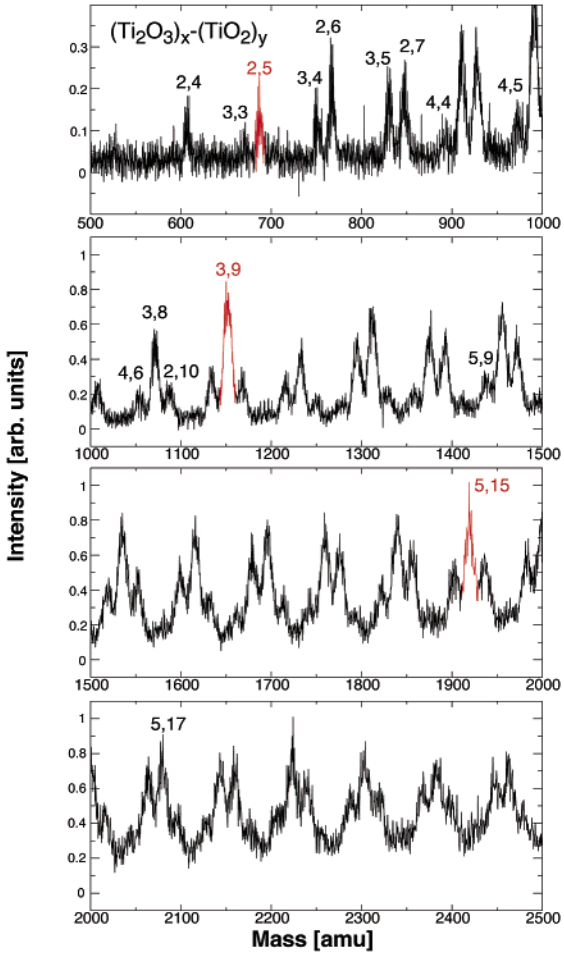

Figure 16. Zoomed in views of the mass spectrum shown in Figure 15. A mass assignment is given in the form *x*,*y*, where *x* and *y* are defined via $(Ti_2O_3)_x-(TiO_2)_y$. Marked in red are peaks for which IR-REMPI spectra are shown in Figure 17.

of the isotope distribution to determine the number of titanium atoms exactly. The peak could thus result from Ti_8O_{14} or, for example, from Ti_7O_{17} or Ti_9O_{11}. Ti_7O_{17} does not seem a likely candidate because clusters with more oxygen than the 1:2 ratio have high ionization potentials.[74] Ti_9O_{11} has a titanium-to-oxygen ratio near 1:1 and could thus have a comparatively low IP. On the other hand, TiO in the bulk is not the preferred composition and one would expect Ti_9O_{11} to be reactive toward oxygen. Thus, if Ti_9O_{11} would be the composition, one would also expect to see clusters such as Ti_9O_{10} or Ti_9O_{12}. Ti_8O_{14} is two oxygen atoms short of $(TiO_2)_8$. In bulk material, oxygen deficiency in TiO_2 is frequently observed and is attributed to sites containing Ti_2O_3. It could well be that the eight titanium containing cluster contains two of those sites and that a better way of writing Ti_8O_{14} would be $(Ti_2O_3)_x$-$(TiO_2)_y$ with $x = 2$ and $y = 4$. Starting with a cluster containing nine titanium atoms, a cluster containing three oxygen atoms less than the 1:2 ratio is observed, $(Ti_2O_3)_x-(TiO_2)_x$ with $x = 3$ and $y = 3$; however with the 16 amu distant ($x = 2$, $y = 5$) cluster being more intense. For clusters containing 11 titanium atoms, the $(Ti_2O_3)_2$ and $(Ti_2O_3)_3$ family become equal in intensity and, for larger clusters, starts to dominate. At 12 titanium atoms, a $(Ti_2O_3)_4-(TiO_2)_n$ progression starts. The $(Ti_2O_3)_2$ progression is no longer visible for clusters with 18 titanium atoms or more. In general, the larger the clusters the more Ti_2O_3 defects are observed.

For each peak in the mass spectrum, the wavelength dependence can be monitored and the resulting IR-REMPI spectra are shown in Figure 17 for three different clusters. The

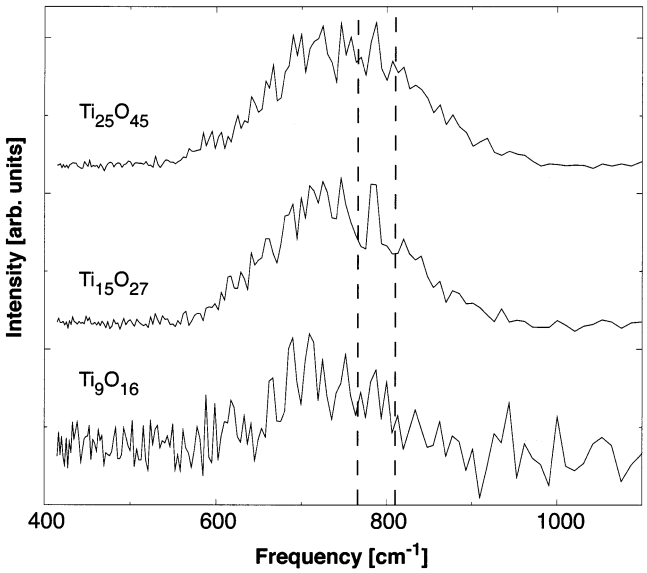

Figure 17. IR-REMPI spectra for three different titanium oxide clusters. Shown as dashed lines is a bulk phonon mode[66] (806 cm^{-1}) and a surface phonon mode[67] (766 cm^{-1}) of bulk TiO_2.

spectra observed for all clusters are characterized by a single almost 200 cm^{-1} broad peak centered around 750 cm^{-1}. No clear dependence on size or number of defects is observed. For rutile TiO_2, bulk and surface phonon modes have been measured. Shown as dashed lines in the figure is a bulk phonon mode[66] at 806 cm^{-1}, measured via IR spectroscopy, and the corresponding surface phonon mode[67] at 766 cm^{-1}, measured by HREELS. Clearly, the surface phonon mode agrees well in position with the IR-REMPI mode(s) of the clusters shown here. In the bulk experiments, resonances are also observed around 400−500 cm^{-1}. We do not find corresponding modes is our experiment. It could be that they are not present, or that they are too weak to be observable in the IR-REMPI experiment. For bulk material, HREELS is also performed on oxygen deficient TiO_2 surfaces that contain Ti_2O_3. It is found that the 766 cm^{-1} mode undergoes a red shift to 710 cm^{-1} and becomes broader when the ratio Ti^{3+}/Ti^{4+} is 0.56.[68] No new modes are found for this material and the spectrum remains qualitatively the same.[68] In Figure 17, the Ti^{3+}/Ti^{4+} ratio is 0.66 for the top two traces and 0.8 for the lowest trace. Nonetheless, the band positions seem to lie closer to the positions of the surface modes of pure TiO_2 rather than to the position of oxygen deficient TiO_2. However, the IR-REMPI bands are broad and could contain more than one unresolved peak such that a peak around 700 cm^{-1} from a defect site and one around 760 cm^{-1} for TiO_2 could be present.

3.2.2.2. Zirconium Oxide Clusters. Zirconium oxide clusters can be generated by laser ablation from a zirconium rod in the presence of the argon carrier gas that contains O_2 (see section 2.3). In fact, the presence of zirconium oxide clusters in the IR-REMPI experiments was first noticed as a nuisance when doing experiments on zirconium carbide clusters. Apparently, traces of oxygen in the carrier gas or in the rod are sufficient to produce zirconium oxide clusters very efficiently. Also, when using plain laboratory air as a carrier gas, zirconium oxide clusters are produced in large abundance. Nonetheless, all data presented here are obtained with a 5% O_2 in argon mixture as a carrier gas.

Figure 18 shows a mass spectrum of zirconium oxide clusters after infrared excitation at 625 cm^{-1}. All peaks result from ions having the composition $Zr_nO_{(2n-1)}^+$. Presumably, clusters that lack one oxygen atom do have a lower IP than clusters having the stoichiometric composition $Zr_nO_{2n}^+$. Similar mass distributions after UV excitation were recently observed by others.[75] The smallest cluster ion observed is ZrO^+. However, as also discussed elsewhere,[35] it is unlikely that this ion results from excitation of neutral ZrO and it is most likely produced by fragmentation of larger ions. The mass spectrum shows pronounced intensity variations. It is, for example, observed that $Zr_{15}O_{29}$ is a cluster that is always more intense than neighboring peaks. This could have to do with either a high stability of the corresponding neutral cluster and/or a low ionization potential.

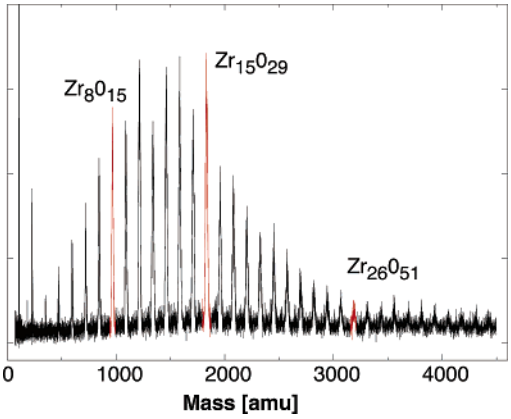

Figure 18. Mass spectrum of zirconium oxide clusters after IR excitation at 625 cm^{-1}. Marked in red are peaks for which IR-REMPI spectra are shown in Figure 19.

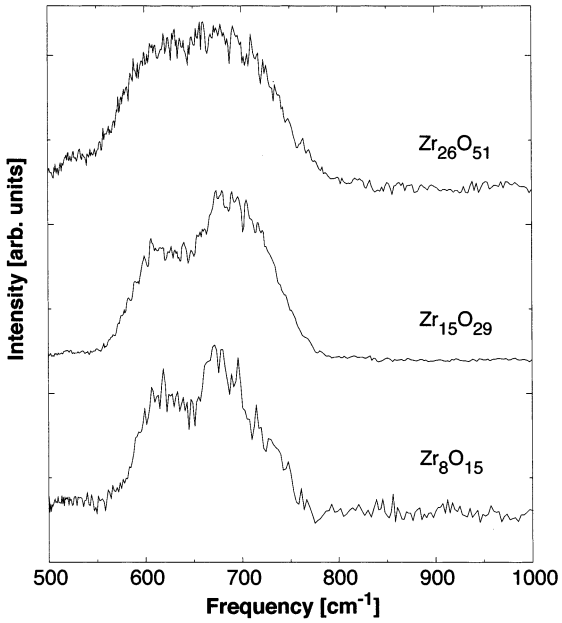

Figure 19. IR-REMPI spectra for three different zirconium oxide clusters.

Figure 19 shows the IR spectra of three zirconium oxide clusters. It is found that all clusters studied show similar spectra: a broad feature consisting of two peaks, one at 620 cm^{-1} and one at 680 cm^{-1}. For larger clusters, the two peaks melt into each other, and for $Zr_{26}O_{51}$, for example, the two features have merged into one broad peak. An IR-REMPI spectrum is also measured when monitoring ZrO^+. The spectrum looks very similar to those shown in Figure 19. However, neutral ZrO is known to have a vibrational frequency of about 900 cm^{-1}.[76] In addition, an efficient multiple photon excitation of a diatomic molecule with FELIX is unlikely, as anhamonicities will shift the resonance outside the spectral profile of FELIX after a few absorbed quanta. The ZrO^+ observed thus does not result from excitation of ZrO. It is also not likely that larger

zirconium oxide cluster ions lose subsequent ZrO_2 fragments to end up at ZrO^+. The loss of a single ZrO_2 unit can be estimated to cost about 8 eV[35] and it is unlikely that a cluster has enough internal energy to lose more than one or two ZrO_2 units. The only possible source of ZrO^+ is then the evaporation of ZrO^+ from large $Zr_nO_{2n-1}^+$ clusters. This might be an inefficient process and most cluster ions might prefer to lose neutral ZrO_2. However, as ZrO^+ from many different cluster sizes will contribute, even a low efficiency per cluster will lead to a large amount of ZrO^+.

The most important question that arises concerns the geometrical structures of the observed clusters. Depending on the temperature, bulk ZrO_2 crystallizes in one of three different phases. Up to 1180 °C the stable structure is monoclinic, between 1180 and 2370 °C a tetragonal phase is formed, and at higher temperatures (up to the melting point of 2600 °C) a cubic structure is preferred. The coordination of the Zr atom in the monoclinic phase is seven whereas it is eight in the tetragonal and cubic phase. Small ZrO_2 particles are known to have a lower transition temperature for the monoclinic to tetragonal phase transition and particles with a radius less than 150 Å are measured to be tetragonal, even at low temperatures.[69,70] The IR spectra of ZrO_2 in its three crystalline phases are distinctively different. As the symmetry of the unit cell is reduced from cubic to tetragonal to monoclinic, more modes become IR allowed. Cubic ZrO_2 has only one IR active mode at 480 cm^{-1},[71] tetragonal ZrO_2 has three IR active modes (575, 435, and 365 cm^{-1})[72] and monoclinic ZrO_2 has 15 IR active modes. The highest frequency mode of these is at 740 cm^{-1} and is characteristic for the monoclinic phase. The other monoclinic modes are situated below 620 cm^{-1}.[72] For the ZrO_2 molecule in a rare gas matrix, the IR active modes are determined to be at 818 and 884 cm^{-1}.[77]

The IR active modes observed here at 620 and 680 cm^{-1} therefore give us no direct information about the symmetry and structure of our clusters. The clusters in the present experiment contain less than 30 Zr atoms. Most of these atoms will be located on or very near the surface of the cluster. It might thus be no surprise that no coincidence with the bulk IR modes of ZrO_2 is observed. Unfortunately, HREELS data on the ZrO_2 surface is not available. Although the spectra presented here are very different from bulk spectra, they compare well to the calculations for small clusters.[35] There, IR active modes are calculated between 600 and 800 cm^{-1} that are characteristic for motion in $(ZrO)_2$ four-membered rings. In addition, the calculations indicate that, at least for clusters with up to four Zr atoms, the preferred structures have connectivities similar to those found in the bulk. It thus seems reasonable that the clusters investigated here also resemble bulk structures and incorporate four-membered ZrO_2 rings.

3.2.3. Zirconium Nitride. Transition metals, such as zirconium, can form not only very strongly bound carbides and oxides but also strongly bound nitrides. Some of those species can have highly interesting properties, such as, for example, superconductivity below a T_c value of 10 K for ZrN. In this context, investigations of the vibrational properties are of special interest. In the bulk, ZrN has a NaCl like fcc structure. For zirconium nitride clusters, one might thus expect similarities with the metal carbide clusters presented here. Here, we will present results from IR-REMPI studies on ZrN clusters. However, we will only give a brief account of some results and the experiments will be discussed in detail in a forthcoming publication.

The experiments are performed in a similar way to those on the carbides and oxides, only that N_2 is used as a source of nitrogen. In Figure 20, two mass spectra are shown. To obtain spectra a shown in the top trace, FELIX is scanned from 1000 to 1050 cm^{-1}, and to obtain mass spectra b, FELIX is scanned from 950 to 1000 cm^{-1}. In both cases, the data are averaged during the scan. Both spectra were part of the same, larger, scan so that the experimental conditions are essentially identical. The structure in the mass spectra is complicated due to the broad isotope distribution of zirconium. An additional complication arises from the presence of a small and seemingly unavoidable contamination with oxygen. In both mass spectra in Figure 20, peaks are observed to appear in groups. The group of peaks around 520 amu (also shown in an expanded view) corresponds to clusters containing five zirconium atoms. To lower masses, groups that correspond to four and three zirconium atoms can be seen. For clusters containing more than six zirconium atoms, the observed peak structure becomes broad and unresolved. Within a group of peaks, the substructure corresponding to different amounts of nitrogen and possibly oxygen atoms can be seen as well as fine structure that results for the zirconium isotopic composition. An oxygen atom is only 2 amu heavier than a nitrogen atom. Compared to this, the zirconium isotope distribution of clusters containing, for example, five zirconium atoms is much broader. It can thus be very difficult to distinguish, for example, $Zr_5N_5^+$ from $Zr_5N_4O^+$.

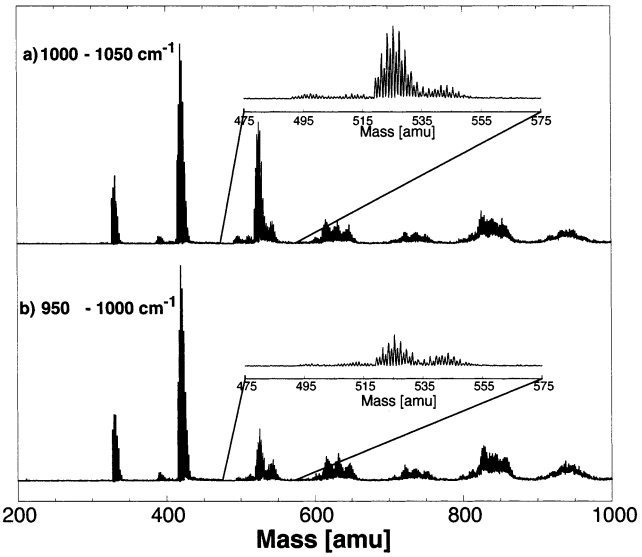

Figure 20. Averaged mass spectra of zirconium nitride clusters while the IR excitation laser was scanned between 1000 and 1050 cm^{-1} (top trace) and between 950 and 1000 cm^{-1} (bottom trace). The ranges corresponding to clusters containing five zirconium atoms are shown zoomed in.

When the two mass spectra are compared, they appear very similar. However, two differences can be clearly seen. First and most pronounced, the most intense group of peaks around 520 amu, containing five zirconium atoms, is much larger in the top spectrum than in the spectrum below. Further, when the spectra, the group of peaks around 495 amu is, although being very weak in both spectra, more intense in the top spectrum as well. Besides those two differences, the mass spectra appear largely identical.

As already mentioned, an assignment of mass peaks to different stoichiometries is difficult. We have chosen to fit the mass spectra to calculated isotope distributions to determine the contributing clusters. Such a fit is done for every wavelength point of FELIX using a linear least squares algorithm. For the sake of efficiency, the mass spectra are binned into 1 amu wide intervals. In the fits presented here, only clusters containing up

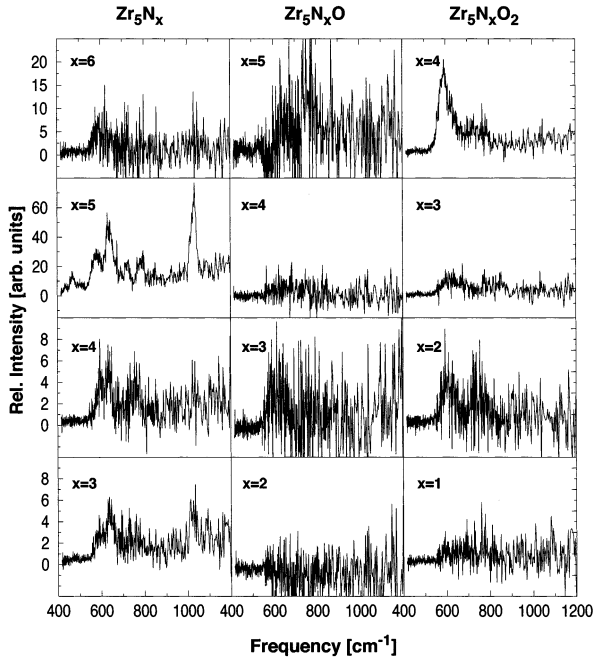

Figure 21. IR-REMPI spectra for twelve possible clusters containing five zirconium atoms. The spectra are the results of a fit and if a spectrum shows only noise around zero; this could mean that (a) no corresponding cluster is in the beam or (b) they do not absorb in that wavelength range or (c) they do not ionize after excitation.

to two oxygen atoms are considered as higher oxygen contents are unlikely and fits showed that if they are present, they are only present in very small amounts. For the rest of the discussion of the zirconium nitride clusters, we focus on the clusters containing five zirconium atoms. The most intense group of peaks for these clusters at around 520 amu could result from $Zr_5N_5^+$, $Zr_5N_4O^+$, and/or $Zr_5N_3O_2^+$.

Figure 21 shows the wavelength dependence in the range 400−1200 cm^{-1} of the twelve species used to fit the cluster distribution (containing five zirconium atoms) between about 490 and 550 amu. The spectra are obtained by a simultaneous and unconstrained fit of the data with the twelve free parameters. Due to this, additional noise is introduced in the wavelength spectra, as noise and fluctuations in the mass spectra can cause a fit, in which one cluster shows a negative intensity, partially compensated by a positive intensity of a cluster with a slightly different mass. Nonetheless, we felt that such an approach is most unbiased. Some of the spectra shown have a clear resolved structure whereas others mainly consist of noise. When the lowest three spectra are reviewed, only Zr_5N_3 and maybe some Zr_5NO_2 are present whereas Zr_5N_2O is most likely not observed and its apparent spectrum shows only noise around zero. In the spectrum of Zr_5N_3, structure can be seen around 600 cm^{-1} and around about 1020 cm^{-1}. The latter peak gives rise to the increase in $Zr_5N_3^+$ around 495 amu in the top trace of Figure 20. In the next higher group of traces, signal is observed for Zr_5N_4 and $Zr_5N_2O_2$ and maybe for Zr_5N_3O. Structure can be seen at around 600 and 750 cm^{-1}. In the next larger group of clusters, the most interesting spectrum can be observed. In the spectrum of Zr_5N_5, at least seven reproducible peaks can be seen. The most intense peak at 1020 cm^{-1} is responsible for the increase for $Zr_5N_5^+$ in the top trace of Figure 20. For the heaviest clusters containing five zirconium atoms and six lighter atoms, $Zr_5N_4O_2$ is the most abundant species. Its spectrum is dominated by a peak around 600 cm^{-1}.

Most IR-REMPI spectra of clusters presented in the preceding sections were unstructured and show one or two broad features. In addition, the variations as a function of cluster size were usually small. The spectra of (oxygen containing) zirconium nitride clusters clearly do not follow this behavior. First, as bulk ZrN has a NaCl like fcc structure, one might expect mass spectra that show intensity variations (magic numbers) similar to those of the mass spectra of the carbides presented in the previous sections. This is not the case and the mass spectra of zirconium nitride clusters do not show the typical nanocrystaline patterns observed for many of the carbides. In addition, the IR-REMPI spectra of the zirconium nitride clusters investigated look very different from the IR-REMPI spectra of the carbides. The most surprising cluster is Zr_5N_5. The large number of resonances imply a low symmetry of the cluster. Nonetheless, it is very abundant in our experiment and apparently very stable. Its strongest resonance at 1020 cm^{-1} is close to the matrix value of the ZrN vibrational frequency of about 980 cm^{-1}.[78] This points to the presence of (at least) one terminal nitrogen atom on the cluster bound to a zirconium atom. Surprisingly, only Zr_5N_5 and most likely also Zr_5N_3 show the presence of a peak at this position. In combination with theoretical calculations, the large number of resonances observed for the Zr_5N_5 cluster should allow an unambiguous identification of its structure.

4. Conclusions and Outlook

Many of the fascinating species that can be produced in the gas phase are so reactive or labile that they will disintegrate or severely change their properties when being in a liquid or solid environment. They can thus only be investigated when being in the gas phase. A technique that is frequently used is mass spectrometry to determine the mass (composition) or mass change (chemical reactivity) of molecules and clusters. Combining mass spectrometry with other technique can give thermodynamic information. Such data, however, yields only limited and indirect structural information. Size information can be obtained by gas-phase ion chromatography.[79]

Optical spectroscopy can be applied for some species. Direct absorption spectroscopy is, however, for most species impractical if not impossible. Measurable properties are the re-emission of photons (fluorescence), mass changes (fragmentation), charge changes (ionization or electron detachment), changes in quantum state that are monitored by resonant photoionization techniques or the direct bolometric measurement of the internal energy. Monitoring a mass or charge change gives the advantage of mass selectivity and very high sensitivity. When such experiments are to be performed in the IR spectral region, usually many more than only one photon need to be absorbed by a single molecule to induce the desired effect. A high power/fluence laser is thus required. When spectroscopic information is desired, wide tunability is required. At present, the only laser that combines those two features is the free electron laser.

Here, we have shown that such an IR laser can induce ionization in strongly bound molecules and clusters. Resonant IR excitation can lead to superhot species that thermally emit an electron. Monitoring the mass selected ion yield as a function of IR laser frequency yields the IR-REMPI spectrum of the molecule or cluster. Although not being the same as the linear absorption spectrum, such an IR-REMPI spectrum can be quite similar and yield valuable information of the IR optical properties of the species investigated.

The IR-REMPI technique is useful to study the IR optical properties of neutral, strongly bound species with comparatively low IPs. When the molecules or clusters of interest are less strongly bound and/or have relatively high IPs, they will not undergo thermionic electron emission after IR excitation and one has to resort to other techniques. One possibility is to

monitor the fragmentation as a function of IR wavelength of either neutral[80] or charged[81] species. For negative ions, electron detachment can be monitored as a function of wavelength, and when the aim is to investigate for example biomolecules or biopolymers, IR induced conformational changes could be monitored by either ionization techniques or gas-phase ion chromatography.

We hope to have shown that multiphoton IR excitation has a bright future for the spectroscopy of gas-phase molecules, clusters, and complexes. Although it requires exotic equipment such as a free electron laser, improvements in nonlinear optical materials and techniques might bring, for a limited spectral range, similar performance to table top systems. At present, however, the very wide tuning range, high pulse energies, and ease of use as well as the reliability that (for FELIX) is comparable to that of standard nanosecond laser systems make FELs the lasers of choice for those studies.

Acknowledgment. We gratefully appreciate the skillful assistance of the FELIX staff, especially that of Lex van der Meer. We also thank M. A. Duncan for a fruitful collaboration and active discussion and Iwan Holleman, Mike Putter, and Boris Sartakov for their efforts in the fullerene experiments. In the metal cluster experiments, we also acknowledge the participation of Andrei Kirilyuk, Andre Fielicke, and Karine Demyk. We also thank Andre van Roij for his role in the construction of the cluster setup. This work is part of the research program of the FOM, which is supported financially by the "Nederlandse organisatie voor Wetenschappelijk Onderzoek" (NWO).

References and Notes

(1) Schultz, A.; Cruse, H. W.; Zare, R. N. *J. Chem. Phys.* **1972**, *57*, 1354.
(2) Ashfold, M. N. R.; Howe, J. D. *Annu. Rev. Phys. Chem.* **1994**, *45*, 57.
(3) Seilmeier, A.; Kaiser, W.; Laubereau, A.; Fischer, S. F. *Chem. Phys. Lett.* **1978**, *58*, 225.
(4) Esherick, P.; Anderson, R. J. M. *Chem. Phys. Lett.* **1980**, *70*, 621.
(5) Seelemann, T.; Andresen, P.; Rothe, E. W. *Chem. Phys. Lett.* **1988**, *146*, 89.
(6) Page, R. H.; Shen, Y. R.; Lee, Y. T. *J. Chem. Phys.* **1988**, *88*, 4621.
(7) Feldmann, D.; Laukemper, J.; Welge, K. H. *J. Chem. Phys.* **1983**, *79*, 278.
(8) Tanabe, S.; Ebata, T.; Fujii, M.; Mikami, N. *Chem. Phys. Lett.* **1993**, *215*, 347.
(9) Pribble, R. N.; Zwier, T. S. *Science* **1994**, *265*, 75.
(10) Putter, M.; von Helden, G.; Meijer, G. *Chem. Phys. Lett.* **1996**, *258*, 118.
(11) Omi, T.; Shitomi, H.; Sekiya, N.; Takazawa, K.; Fujii, M. *Chem. Phys. Lett.* **1996**, *252*, 287.
(12) Mons, M.; Robertson, E. G.; Snoek, L. C.; Simons, J. P. *Chem. Phys. Lett.* **1999**, *310*, 423.
(13) Bagratashvili, V. N.; Letokhov, V. S.; Makarov, A. A.; Ryabov, E. A. *Multiple Photon Infrared Laser Photophysics and Photochemistry*; Harwood Academic Publishers: Chur, 1985.
(14) Makowe, J.; Boyarkin, O. V.; Rizzo, T. R. *J. Phys. Chem. A* **2002**, *106*, 5221.
(15) Fuss, W.; Göthel, J.; Ivanenko, M.; Schmid, W. E.; Hering, P.; Kompa, K. L.; Witte, K. *Isotolpenpraxis Environ. Health Studies* **1994**, *30*, 199.
(16) Grant, E. R.; Schulz, P. A.; Sudbo, A. S.; Shen, Y. R.; Lee, Y. T. *Phys. Rev. Lett.* **1978**, *40*, 115.
(17) Fuss, W. *Chem. Phys.* **1979**, *36*, 135.
(18) Fuss, W.; Kompa, K. L. *Prog. Quant. Electr.* **1981**, *7*, 117.
(19) Hippler, M.; Quack, M.; Schwarz, R.; Seyfang, G.; Matt, S.; Märk, T. *Chem. Phys. Lett.* **1997**, *278*, 111.
(20) Bagratashvili, V. N.; Kuzmin, M. V.; Letokhov, V. S.; Shibanov, A. N. *JETP Lett.* **1983**, *37*, 112.
(21) Campbell, E. E. B.; Ulmer, G.; Hertel, I. V. *Phys. Rev. Lett.* **1991**, *67*, 1986.
(22) Wurz, P.; Lykke, K. R. *J. Chem. Phys.* **1991**, *95*, 7008.
(23) Campbell, E. E. B.; Levine, R. D. *Annu. Rev. Phys. Chem.* **2000**, *51*, 65.
(24) Amrein, A.; Simpson, R.; Hackett, P. *J. Chem. Phys.* **1991**, *95*, 1781.
(25) Leisner, T.; Athanassenas, K.; Echt, O.; Kandler, O.; Kreisle, D.; Recknagel, E. *Z. Phys. D* **1991**, *20*, 127.
(26) Leisner, T.; Athanassenas, K.; Kreisle, D.; Recknagel, E.; Echt, O. *J. Chem. Phys.* **1993**, *99*, 9670.
(27) May, B. D.; Cartier, S. F.; Castleman, J. A. W. *Chem. Phys. Lett.* **1995**, *242*, 265.
(28) von Helden, G.; Holleman, I.; Knippels, G. M. H.; van der Meer, A. F. G.; Meijer, G. *Phys. Rev. Lett.* **1997**, *79*, 5234.
(29) von Helden, G.; Holleman, I.; van Roij, A. J. A.; Knippels, G. M. H.; van der Meer, A. F. G.; Meijer, G. *Phys. Rev. Lett.* **1998**, *81*, 1825.
(30) von Helden, G.; Holleman, I.; Putter, M.; van Roij, A. J. A.; Meijer, G. *Chem. Phys. Lett.* **1999**, *299*, 171.
(31) von Helden, G.; Holleman, I.; Meijer, G.; Sartakov, B. *Opt. Exp.* **1999**, *4*, 46.
(32) van Heijnsbergen, D.; von Helden, G.; Duncan, M. A.; van Roij, A. J. A.; Meijer, G. *Phys. Rev. Lett.* **1999**, *83*, 4983.
(33) von Helden, G.; Tielens, A. G. G. M.; van Heijnsbergen, D.; Duncan, M. A.; Hony, S.; Waters, L. B. F. M.; Meijer, G. *Science* **2000**, *288*, 313.
(34) van Heijnsbergen, D.; von Helden, G.; Sartakov, B.; Meijer, G. *Chem. Phys. Lett.* **2000**, *321*, 508.
(35) von Helden, G.; Kirilyuk, A.; van Heijnsbergen, D.; Sartakov, B.; Duncan, M. A.; Meijer, G. *Chem. Phys.* **2000**, *262*, 31.
(36) von Helden, G.; van Heijnsbergen, D.; Duncan, M. A.; Meijer, G. *Chem. Phys. Lett.* **2001**, *333*, 350.
(37) van Heijnsbergen, D.; von Helden, G.; Meijer, G.; Duncan, M. A. *J. Chem. Phys.* **2002**, *116*, 2400.
(38) van Heijnsbergen, D.; Fielicke, A.; Meijer, G.; von Helden, G. *Phys. Rev. Lett.* **2002**, *89*, 013401.
(39) Oepts, D.; van der Meer, A. F. G.; van Amersfoort, P. W. *Infrared Phys. Technol.* **1995**, *36*, 297.
(40) Knippels, G. M. H.; Mols, R. F. X. A. M.; van der Meer, A. F. G.; Oepts, D.; van Amersfoort, P. W. *Phys. Rev. Lett.* **1995**, *75*, 1755.
(41) Freund, H. P.; Antonsen, J. T. M. *Principles of Free-electron Lasers*; Chapman & Hall: London, 1992.
(42) Wurz, P.; Lykke, K. R. *J. Phys. Chem.* **1992**, *96*, 10129.
(43) Bethune, D. S.; Meijer, G.; Tang, W. C.; Rosen, H. J.; Golden, W. G.; Seki, H.; Brown, C. A.; de Vries, M. S. *Chem. Phys. Lett.* **1991**, *179*, 181.
(44) Wang, K.-A.; Rao, A. M.; Eklund, P. C.; Dresselhaus, M. S.; Dresselhaus, G. *Phys. Rev. B* **1993**, *48*, 11375.
(45) Nemes, L.; Ram, R. S.; Bernath, P. F.; Tinker, F. A.; Zumwalt, M. C.; Lamb, L. D.; Huffman, D. R. *Chem. Phys. Lett.* **1994**, *218*, 295.
(46) Holleman, I.; Boogaarts, M. G. H.; van Bentum, P. J. M.; Meijer, G. *Chem. Phys. Lett.* **1995**, *240*, 165.
(47) Fowler, P. W.; Manolopoulos, D. E. *An Atlas of Fullerenes*; Oxford University Press: Oxford, U.K., 1995.
(48) Diederich, F.; Ettl, R.; Rubin, Y.; Whetten, R. L.; Beck, R.; Alvarez, M.; Anz, S.; Sensharma, D.; Wudl, F.; Khemani, K. C.; Koch, A. *Science* **1991**, *252*, 548.
(49) Kikuchi, K.; Nakahara, N.; Wakabayashi, T.; Suzuki, S.; Shiromaru, H.; Miyake, Y.; Saito, K.; Ikemoto, I.; Kainosho, M.; Achiba, Y. *Nature* **1992**, *357*, 142.
(50) Schettino, V.; Salvi, P. R.; Bini, R.; Cardini, G. *J. Chem. Phys.* **1994**, *101*, 11079.
(51) Guo, B. C.; Kerns, K. P.; Castleman, A. W. J. *Science* **1992**, *255*, 1411.
(52) Pilgrim, J. S.; Duncan, M. A. *J. Am. Chem. Soc.* **1993**, *115*, 9724.
(53) Duncan, M. A. *J. Cluster Sci.* **1997**, *8*, 239.
(54) Dance, I. *J. Chem. Soc., Chem. Commun.* **1992**, 1779.
(55) Dance, I. *J. Am. Chem. Soc.* **1996**, *118*, 6309.
(56) Rohmer, M.-M.; Benard, M.; Henriet, C.; Bo, C.; Poblet, J.-M. *J. Chem. Soc., Chem. Commun.* **1993**, *1993*, 1182.
(57) Benard, M.; Rohmer, M.-M.; Poblet, J.-M.; Bo, C. *J. Phys. Chem.* **1995**, *99*, 16913.
(58) Rohmer, M.-M.; Bo, C.; Poblet, J.-M. *J. Am. Chem. Soc.* **1995**, *117*, 508.
(59) Gueorguiev, G. K.; Pacheco, J. M. *Phys. Rev. Lett.* **2002**, *88*, 115504.
(60) Wei, S.; Guo, B. C.; Purnell, J.; Buzza, S.; Castleman, A. W. J. *Science* **1992**, *256*, 818.
(61) Wei, S.; Castleman, A. W. J. *Chem. Phys. Lett.* **1994**, *227*, 305.
(62) Oshima, C.; Aizawa, T.; Wuttig, M.; Souda, R.; Otani, S.; Ishizawa, Y. *Phys. Rev. B* **1987**, *36*, 7510.
(63) Kwok, S.; Volk, K.; Hrivnak, J. *Astrophys. J.* **1989**, *345*, L51.
(64) Bernatowicz, T. J.; Cowsik, R.; Gibbons, P. C.; Lodders, K.; Fegley, B., Jr.; Amari, S.; Lewis, R. S. *Astrophys. J.* **1996**, *472*, 760.
(65) Waters, L. B. F. M.; Molster, F. J.; de Jong, T.; Beintema, D. A.; Waelkens, C.; Boogert, A. C. A.; Boxhoorn, D. R.; de Graauw, T.; Drapatz, S.; Feuchtgruber, H.; Genzel, R.; Helmich, F. P.; Heras, A. M.; Huygen, R.; Izumiura, H.; Justtanont, K.; Kester, D. J. M.; Kunze, D.; Lahuis, F.;

Lamers, H. J. G. L. M.; Leech, K. J.; Loup, C.; Lutz, D.; Morris, P. W.; Price, S. D.; Roelfsema, P. R.; Salama, A.; Schaeidt, S. G.; Tielens, A. G. G. M.; Trams, N. R.; Valentijn, E. A.; Vandenbussche, B.; van den Ancker, M. E.; van Dishoeck, E. F.; Van Winckel, H.; Wesselius, P. R.; Young, E. T. *Astron. Astrophys.* **1996**, *315*, L361.

(66) Eagles, D. M. *J. Phys. Chem. Solids* **1964**, *25*, 1234.

(67) Kesmodel, L. L.; Gates, J. A.; Chung, Y. W. *Phys. Rev. B* **1981**, *23*, 489.

(68) Eriksen, S.; Egdell, R. G. *Surf. Sci.* **1987**, *180*, 263.

(69) Garvie, R. C. *J. Phys. Chem.* **1965**, *69*, 1238.

(70) Garvie, R. C. *J. Phys. Chem.* **1978**, *82*, 218.

(71) Phillippi, C. M.; Mazdiyasni, K. S. *J. Am. Ceram. Soc.* **1971**, *54*, 254.

(72) Feinberg, A.; Perry, C. H. *J. Phys. Chem. Solids* **1981**, *42*, 513.

(73) Thomas, O. C.; Xu, S.; Lippa, T. P.; Bowen, K. H., Jr. *J. Cluster Sci.* **1999**, *10*, 515.

(74) Albaret, T.; Finocchi, F.; Noguera, C. *J. Chem. Phys.* **2000**, *113*, 2238.

(75) Foltin, M.; Stueber, G. J.; Bernstein, E. R. *J. Chem. Phys.* **2001**, *114*, 8971.

(76) Herzberg, G. *Molecular Spectra and Molecular Structure II Infrared and Raman Spectra of Polyatomic Molecules*; van Nostrand-Reinhold: New York, 1945.

(77) Chertihin, G. V.; Andrews, L. *J. Phys. Chem.* **1995**, *99*, 6356.

(78) Kushto, G. P.; Souter, P. F.; Chertihin, G. V.; Andrews, L. *J. Chem. Phys.* **1999**, *110*, 9020.

(79) von Helden, G.; Hsu, M.-T.; Kemper, P. R.; Bower, M. T. *J. Chem. Phys.* **1991**, *95*, 3835.

(80) Simard, B.; Dénommée, S.; Rayner, D. M.; van Heijnsbergen, D.; Meijer, G.; von Helden, G. *Chem. Phys. Lett.* **2002**, *157*, 195.

(81) Oomens, J.; Meijer, G.; von Helden, G. *J. Phys. Chem. A* **2001**, *105*, 8302.